JETP Letters, Vol. 72, No. 1, 2000, pp. 1–3. From Pis'ma v Zhurnal Éksperimental'noĭ i Teoreticheskoĭ Fiziki, Vol. 72, No. 1, 2000, pp. 3–7.

Relative Phase between the $J/\psi \longrightarrow \rho\eta$ and $\omega\eta$ Amplitudes[1]

N. N. Achasov and V. V. Gubin

Laboratory of Theoretical Physics, Sobolev Institute of Mathematics, Siberian Division, Russian Academy of Sciences, pr. Akademika Kortyuga 4, Novosibirsk, 630090 Russia
e-mail: achasov@math.nsc.ru; gubin@math.nsc.ru

Received April 18, 2000; in final form, May 25, 2000

It is shown that the study of the ω–ρ^0 interference pattern in $J/\psi \longrightarrow (\rho^0 + \omega)\eta \longrightarrow \pi^+\pi^-\eta$ decay provides evidence for a large (nearly 90°) relative phase between the one-photon and the three-gluon decay amplitudes.
© 2000 MAIK "Nauka/Interperiodica".

PACS numbers: 13.25.Gv; 11.30.Hv; 13.40.Hq; 14.40.Gx

In the last few years, it has been noted that the single-photon and three-gluon amplitudes in two-body $J/\psi \longrightarrow 1^-0^-$ and $J/\psi \longrightarrow 0^-0^-$ [1–3] decays appear to have relative phases of nearly 90°.

This unexpected result is very important to the observability of CP violating decays, as well as to the nature of the $J/\psi \longrightarrow 1^-0^-$ and $J/\psi \longrightarrow 0^-0^-$ decays [1–6]. In particular, it points to the nonadequacy of their description built upon perturbative QCD, the hypothesis of the factorization of short and long distances, and specified wave functions of final hadrons. Some peculiarities of electromagnetic form factors in the J/ψ mass region were discussed in [7].

The analysis [1–3] involved theoretical assumptions relying on the strong interaction $SU_f(3)$-symmetry, the strong interaction $SU_f(3)$-symmetry breaking, and the SU_f (3) transformation properties of the one-photon annihilation amplitudes. In addition, the effects of ρ–ω mixing in the $J/\psi \longrightarrow 1^-0^-$ decays were not taken into account in [1], while in [2], ρ–ω mixing was taken into account incorrectly; see the discussion below. Because of this, model-independent determination of these phases is required.

Fortunately, it is possible to check the conclusion of [1, 2] at least in one case. We mean the phases between the amplitudes of the one-photon $J/\psi \longrightarrow \rho^0\eta$ and three-gluon $J/\psi \longrightarrow \omega\eta$ decays.

Indeed, the $\omega - \rho$ interference pattern in the $J/\psi \longrightarrow (\rho^0 + \omega)\eta \longrightarrow \rho^0\eta \longrightarrow \pi^+\pi^-\eta$ decay is conditioned by ρ^0–ω mixing and the ratio of the amplitudes of ρ^0 and ω production. As for the ρ^0–ω mixing amplitude, it is reasonably well studied [8–14]. Its module and phase are known. The module of the ratio of the amplitudes of ρ and ω production can be obtained from the data on the branching ratios of the J/ψ-decays. Thus, the interference pattern provides a way of measuring the relative phases of the ρ^0 and ω production amplitudes.

[1]This article was submitted by the authors in English.

The $\pi^+\pi^-$-spectrum in the ω, ρ energy region is of the form

$$\frac{dN}{dm} = N_\rho(m)\frac{2}{\pi}m\Gamma(\rho \longrightarrow \pi\pi, m)\left|\frac{1}{D_\rho(m)}\right.$$
$$+ \frac{\Pi_{\omega\rho^0}(m)}{D_\rho(m)D_\omega(m)}\left[\frac{N_\omega(m)}{N_\rho(m)}\right]^{1/2}\exp\{i(\delta_\omega - \delta_\rho)\} \qquad (1)$$
$$\left. + \frac{1}{D_\omega(m)}\frac{g_{\omega\pi\pi}}{g_{\rho\pi\pi}}\left[\frac{N_\omega(m)}{N_\rho(m)}\right]^{1/2}\exp\{i(\delta_\omega - \delta_\rho)\}\right|^2,$$

where m is the invariant mass of the $\pi^+\pi^-$ state; $N_\rho(m)$ and $N_\omega(m)$ are the squares of the modules of the ρ and ω production amplitudes; δ_ρ and δ_ω are their phases; $\Pi_{\omega\rho^0}(m)$ is the amplitude of the ρ–ω transition; and $D_V(m) = m_V^2 - m^2 - im\Gamma_V(m)$, $V = \rho, \omega$.

In the discussion that follows, Eq. (1) is conveniently rewritten as

$$\frac{dN}{dm} = N_\rho(m)\frac{2}{\pi}m\Gamma(\rho \longrightarrow \pi\pi, m)\left|\frac{1}{D_\rho(m)}\right.$$
$$\times\left(1 - \varepsilon(m)\left[\frac{N_\omega(m)}{N_\rho(m)}\right]^{1/2}\exp\{i(\delta_\omega - \delta_\rho)\}\right)$$
$$+ \frac{1}{D_\omega(m)}(\varepsilon(m) + g_{\omega\pi\pi}/g_{\rho\pi\pi}) \qquad (2)$$
$$\left.\times\left[\frac{N_\omega(m)}{N_\rho(m)}\right]^{1/2}\exp\{i(\delta_\omega - \delta_\rho)\}\right|^2,$$

where

$$\varepsilon(m) = -\frac{\Pi_{\omega\rho^0}(m)}{m_\omega^2 - m_\rho^2 + im(\Gamma_\rho(m) - \Gamma_\omega(m))}. \qquad (3)$$

As is known [8–12], the imaginary part of the ρ–ω transition amplitude is due to the ππ, 3π, γπ, and γη intermediate states:

$$\mathrm{Im}(\Pi_{\rho^0\omega}(m)) = m\Bigg(\frac{g_{\omega\pi\pi}}{g_{\rho\pi\pi}}\Gamma(\rho \longrightarrow \pi\pi, m) + \frac{g_{\rho\rho\pi}}{g_{\omega\rho\pi}}\Gamma(\omega \longrightarrow \rho\pi \longrightarrow 3\pi, m) + \frac{g_{\rho\gamma\pi}}{g_{\omega\gamma\pi}}\Gamma(\omega \longrightarrow \gamma\pi, m_\omega) + \frac{g_{\rho\gamma\eta}}{g_{\omega\gamma\eta}}\Gamma(\omega \longrightarrow \gamma\eta, m)\Bigg). \quad (4)$$

A quite conservative estimate of the contribution of the ππ and 3π intermediate states gives

$$m_\omega\frac{g_{\omega\pi\pi}}{g_{\rho\pi\pi}}\Gamma(\rho \longrightarrow \pi\pi, m_\omega) = \pm m_\omega \times 10^{-2}\Gamma(\rho \longrightarrow \pi\pi, m_\omega) = 1.17 \times 10^{-3}\ \mathrm{GeV}^{-2},$$
$$m_\omega\frac{g_{\rho\rho\omega}}{g_{\omega\rho\pi}}\Gamma(\omega \longrightarrow \rho\pi \longrightarrow 3\pi, m_\omega) = \pm m_\omega \times 10^{-2}\Gamma(\omega \longrightarrow 3\pi, m_\omega) = \pm 5.84 \times 10^{-5}\ \mathrm{GeV}^{-2}. \quad (5)$$

The constituent quark and vector meson dominance models both give the same result:

$$m_\omega\frac{g_{\rho\gamma\pi}}{g_{\omega\gamma\pi}}\Gamma(\omega \longrightarrow \gamma\pi, m_\omega) = m_\omega \times \frac{1}{3}\Gamma(\omega \longrightarrow \gamma\pi, m_\omega) = 1.86 \times 10^{-4}\ \mathrm{GeV}^{-2},$$
$$m_\omega\frac{g_{\rho\gamma\eta}}{g_{\omega\gamma\pi}}\Gamma(\omega \longrightarrow \gamma\eta, m_\omega) = m_\omega \times 3\Gamma(\omega \longrightarrow \gamma\eta, m_\omega) = 1.28 \times 10^{-5}\ \mathrm{GeV}^{-2}. \quad (6)$$

Notice that the predictions of the constituent quark and vector meson dominance models on the $\rho \longrightarrow \gamma\pi(\eta)$ and $\omega \longrightarrow \gamma\pi(\eta)$ decays agree adequately with the experiment.

As is seen from Eqs. (3) and (4), the contribution of the ππ intermediate state in $\mathrm{Im}(\Pi_{\omega\rho^0}(m))$ and the $g_{\omega\pi\pi}$ direct coupling constant cancel considerably in the $g^{\mathrm{eff}}_{\omega\pi\pi}$ effective coupling constant:

$$g^{\mathrm{eff}}_{\omega\pi\pi}(m) = \varepsilon(m)g_{\rho\pi\pi} + g_{\omega\pi\pi} = -\frac{\Pi'_{\omega\rho^0}(m)g_{\rho\pi\pi} + i\Gamma(\rho \longrightarrow \pi\pi, m)g_{\omega\pi\pi}}{m_\omega^2 - m_\rho^2 + im(\Gamma_\rho(m) - \Gamma_\omega(m))} + g_{\omega\pi\pi}$$
$$= \frac{\Pi'_{\omega\rho^0}(m) + (m_\rho^2 - m_\omega^2 + im\Gamma_\omega(m))(g_{\omega\pi\pi}/g_{\rho\pi\pi})}{m_\omega^2 - m_\rho^2 + im(\Gamma_\rho(m) - \Gamma_\omega(m))}g_{\rho\pi\pi} \quad (7)$$
$$= -\frac{\Pi'_{\omega\rho^0}(m) \mp 1.87 \times 10^{-4}\ \mathrm{GeV}^{-2} \pm i6.6 \times 10^{-5}\ \mathrm{GeV}^{-2}}{m_\omega^2 - m_\rho^2 + im(\Gamma_\rho(m) - \Gamma_\omega(m))}g_{\rho\pi\pi},$$

where $\Pi'_{\omega\rho^0}(m)$ is the amplitude of the ρ^0–ω transition without the contribution of the ππ intermediate state in the imaginary part; the numerical values are calculated at $m = m_\omega$.

The branching ratio of the $\omega \longrightarrow \pi\pi$ decay is

$$B(\omega \longrightarrow \pi\pi) = \frac{\Gamma(\rho \longrightarrow \pi\pi, m_\omega)}{\Gamma_\omega(m_\omega)} \times \left|\varepsilon(m_\omega) + g_{\omega\pi\pi}/g_{\rho\pi\pi}\right|^2. \quad (8)$$

It follows from Eqs. (6) and (7) that the imaginary part of the numerator in Eq. (7) is dominated by the γπ intermediate state to within 35%. This imaginary part gives $B(\omega \longrightarrow \pi\pi) \simeq 5 \times 10^{-5}$ instead of the experimental value [14]

$$B(\omega \longrightarrow \pi^+\pi^-) = 0.0221 \pm 0.003. \quad (9)$$

Thus, one can get the module of the real part of the numerator in Eq. (7), which is clearly dominated by $\mathrm{Re}(\Pi_{\omega\rho^0}(m))$. In addition, the interference pattern of the ρ^0 and ω mesons in the $e^+e^- \longrightarrow \pi^+\pi^-$ reaction and in $\pi^+\pi^-$ photoproduction on nuclei shows [8–12] that the real part of the numerator in Eq. (7) is positive. Thus, from Eqs. (3), (7), (8), and (9) one gets

$$\mathrm{Re}(\Pi_{\rho^0\omega}(m_\omega)) = (3.80 \pm 0.27) \times 10^{-3}\ \mathrm{GeV}^2 \quad (10)$$

and

$$\varepsilon(m_\omega) + g_{\omega\pi\pi}/g_{\rho\pi\pi} = (3.41 \pm 0.24) \times 10^{-2}\exp\{i(102 \pm 1)^\circ\}. \quad (11)$$

The data [15, 16] were fitted with the function

$$N(m) = L(m) + \left|(N_\rho)^{1/2}F_\rho^{BW}(m) + (N_\omega)^{1/2}F_\omega^{BW}(m)\exp\{i\phi\}\right|^2, \quad (12)$$

where $F_\rho^{BW}(m)$ and $F_\omega^{BW}(m)$ are the appropriate Breit–Wigner terms [15] and $L(m)$ is a polynomial background term.

The results are

$$\phi = (46 \pm 15)^\circ, \quad N_\omega(m_\omega)/N_\rho = 8.86 \pm 1.83\ \ [15],$$
$$\phi = -0.08 \pm 0.17 = (-4.58 \pm 9.74)^\circ, \quad (13)$$
$$N_\omega(m_\omega)/N_\rho = 7.37 \pm 1.72\ \ [16].$$

From Eqs. (2), (8), and (12) it follows that

$$N_\rho = N_\rho(m_\rho) \times \left|1 - \varepsilon(m_\rho)[N_\omega(m_\rho)/N_\rho(m_\rho)]^{1/2}\exp\{i(\delta_\omega - \delta_\rho)\}\right|^2, \quad (14)$$

$$N_\omega = B(\omega \longrightarrow \pi\pi)N_\omega(m_\omega), \quad (15)$$

$$\phi = \delta_\omega - \delta_\rho + \arg[\varepsilon(m_\omega) + g_{\omega\pi\pi}/g_{\rho\pi\pi}]$$
$$- \arg\{1 - \varepsilon(m_\rho)[N_\omega(m_\rho)/N_\rho(m_\rho)]^{1/2}\exp\{i(\delta_\omega - \delta_\rho)\}\}$$
$$\simeq \delta_\omega - \delta_\rho + \arg[\varepsilon(m_\omega) + g_{\omega\pi\pi}/g_{\rho\pi\pi}] \quad (16)$$
$$- \arg\{1 - |\varepsilon(m_\omega)|[N_\omega(m_\omega)/N_\rho]^{1/2}\exp\{i\phi\}\}.$$

From Eqs. (11), (13) and (16) we get that

$$\delta_\rho - \delta_\omega = \delta_\gamma = (60 \pm 15)^\circ \text{ [15]}, \quad (17)$$

$$\delta_\rho - \delta_\omega = \delta_\gamma = (106 \pm 10)^\circ \text{ [16]}. \quad (18)$$

A large (nearly 90°) δ_γ was obtained in [1, 2]. Thus, both the MARK III Collaboration [15] and the DM2 Collaboration [16], see Eqs. (17) and (18), provide support for this view.

The DM2 Collaboration used statistics only half as high as the MARK III Collaboration, but, in contrast to the MARK III Collaboration, which fitted N_ω as a free parameter, the DM2 Collaboration calculated it from the branching ratio of $J/\psi \longrightarrow \omega\eta$ using Eq. (15).

In [2], the effect of the ρ–ω transition in the $J/\psi \longrightarrow \omega\pi^0$ decay is neglected, for it is assumed that this effect is less significant than in the $J/\psi \longrightarrow \rho\eta$ decay. Actually, the effect of the ρ–ω transition on the $J/\psi \longrightarrow \omega\pi^0$ decay intensity is

$$\overline{N}_\omega \simeq \overline{N}_\omega(m_\omega) \quad (19)$$
$$\times \left|1 + \varepsilon(m_\omega)[\overline{N}_\rho(m_\omega)/\overline{N}_\omega(m_\omega)]^{1/2}\exp\{i(\bar{\delta}_\rho - \bar{\delta}_\omega)\}\right|^2,$$

where $\overline{N}_\omega(m_\omega)$ and $\overline{N}_\rho(m_\omega)$ are the squares of the modules of the $J/\psi \longrightarrow \omega\pi^0$ and $J/\psi \longrightarrow \rho\pi^0$ amplitudes and $\bar{\delta}_\omega$ and $\bar{\delta}_\rho$ are their phases. In [1, 2], it is suggested that $\delta_\rho - \delta_\omega = \bar{\delta}_\omega - \bar{\delta}_\rho = \delta_\gamma$. Experimentally [14], $\overline{N}_\rho(m_\omega)/\overline{N}_\omega(m_\omega) \simeq 10$. Thus, the corrections due to the ρ–ω transition in Eqs. (14) and (19) have approximately equal modules. For $\delta_\gamma = 90^\circ$ they are equal to approximately 20% but are opposite in sign. It is significant that $\overline{N}_\omega$ and N_ρ are measured with an accuracy of 14% and 12%, respectively. In [2], it was mistakenly assumed that the ρ contribution was not isolated from the $J/\psi \longrightarrow (\rho + \omega)\eta \longrightarrow \pi^+\pi^-\eta$ decay. The isolation was done there by some means, and a magnitude of $N_\rho(m_\rho)$ was obtained which differed from the true one by three standard deviations.

In summary, we should emphasize that it is urgent to study this fundamental problem once again with BES in Beijing. Needless to say, the τ-CHARM factory [14] would solve this problem in an exhaustive way.

We thank G.F. Xu very much for discussions. This work was supported in part by the INTAS-RFBR, grant IR-97-232.

REFERENCES

1. G. López Castro, J. L. Lucio M., and J. Pestieau, AIP Conf. Proc. **342**, 441 (1995); hep-ph/9902300.
2. M. Suzuki, Phys. Rev. D **57**, 5717 (1998).
3. M. Suzuki, Phys. Rev. D **60**, 051501 (1999).
4. J. L. Rosner, Phys. Rev. D **60**, 074029 (1999).
5. Y. F. Gu and S. F. Tuan, in *HADRON 99, Beijing, August 24–28, 1999*; hep-ph/9910423.
6. J.-M. Gerard and J. Weyers, Phys. Lett. B **462**, 324 (1999).
7. N. N. Achasov and A. A. Kozhevnikov, Phys. Rev. D **58**, 097502 (1998); Yad. Fiz. **62**, 364 (1999) [Phys. At. Nucl. **62**, 328 (1999)].
8. A. S. Goldhaber, G. S. Fox, and C. Quigg, Phys. Lett. B **30**, 249 (1969).
9. M. Gourdin, L. Stodolsky, and F. M. Renard, Phys. Lett. B **30**, 347 (1969).
10. F. M. Renard, Nucl. Phys. B **15**, 118 (1970).
11. N. N. Achasov and G. N. Shestakov, Nucl. Phys. B **45**, 93 (1972); Fiz. Élem. Chastits At. Yadra **9**, 48 (1978) [Sov. J. Part. Nucl. **9**, 19 (1978)].
12. N. N. Achasov and A. A. Kozhevnikov, Yad. Fiz. **55**, 809 (1992) [Sov. J. Nucl. Phys. **55**, 449 (1992)]; Int. J. Mod. Phys. A **7**, 4825 (1992).
13. N. N. Achasov, A. A. Kozhevnikov, and G. N. Shestakov, Phys. Lett. B **50**, 448 (1974); N. N. Achasov, N. M. Budnev, A. A. Kozhevnikov, and G. N. Shestakov, Yad. Fiz. **23**, 610 (1976) [Sov. J. Nucl. Phys. **23**, 320 (1976)].
14. C. Caso *et al.* (Particle Data Group), Eur. Phys. J. C **3**, 1 (1998).
15. D. Coffman *et al.*, Phys. Rev. D **38**, 2695 (1988).
16. J. Jousset *et al.*, Phys. Rev. D **41**, 1389 (1990).

JETP Letters, Vol. 72, No. 1, 2000, pp. 11–13. Translated from Pis'ma v Zhurnal Éksperimental'noĭ i Teoreticheskoĭ Fiziki, Vol. 72, No. 1, 2000, pp. 18–22.

On the Possibility of "Informational" Cooling of Neutral Atoms

V. I. Balykin* and V. S. Letokhov

Institute of Spectroscopy, Russian Academy of Sciences, Troitsk, Moscow region, 142190 Russia
**e-mail: balykin@isan.troitsk.ru*

Received May 25, 2000

A method of lowering the temperature of neutral atoms is considered. The method is based on gaining information on the translational state of individual atoms and the use of this information for the separation of slow and fast atoms. The lowest attainable temperature of an atomic ensemble is appreciably lower than the atomic recoil energy. © *2000 MAIK "Nauka/Interperiodica".*

PACS numbers: 32.80.Pj

The presently existing methods of cooling neutral and charged particles are based on the use of various dissipative processes. For example, electron cooling of charged particles [1] is accomplished through the collisions of hot ions with cold electron gas, resulting in the dissipation of thermal ion energy to the cold electrons. This method has found wide use in enhancing the phase density of high-velocity ion beams in storage rings [2]. The most developed method of cooling neutral atoms (as well as localized ions) is based on the inelastic collisions of neutral atoms with laser photons [3]. Laser cooling of atoms made it possible to observe the Bose–Einstein condensation of neutral atoms [4].

The method suggested in this work for lowering the temperature of neutral atoms is based on gaining information on the translational state (coordinates and velocities) of individual atoms and using this information for the separation of slow and fast atoms. This, in turn, reduces the temperature for part of the initial atomic ensemble and, correspondingly, increases its phase density. This method can be called "informational cooling of neutral atoms." Note that there is a certain analogy of the proposed method with the old idea of the Maxwell demon [5], as well as with the method of stochastic cooling of fast ions in storage rings [6].

The idea of the method of informational cooling of neutral atoms is illustrated in the figure. Let the atoms be initially located in one of the atomic traps (*1*) connected by atomic waveguide (*3*). The traps and waveguide may be, e.g., magnetic or optical of the dipolar type (see reviews [7, 8]). The atoms can transfer from one trap to the other through the waveguide. The waveguide is

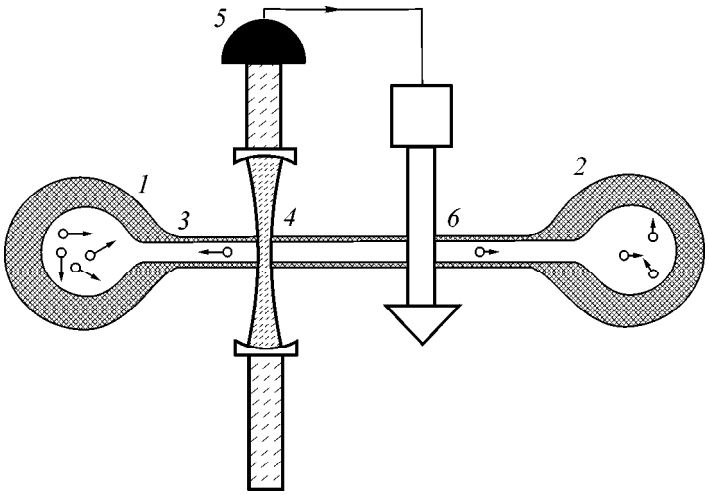

Schematic representation of two atomic traps (*1*, *2*) connected by atomic waveguide (*3*). Laser beam (*4*) crosses the atomic trajectories in the waveguide and serves to gain information in detector (*5*) on the translational atomic state to control the operation of optical gate (*6*) based on the dipolar strength.

0021-3640/00/7201-0011$20.00 © 2000 MAIK "Nauka/Interperiodica"

crossed by a laser beam (*4*), which plays the role of a reading device in detector (*5*) to gain information about the atoms. The information is transmitted to the optical gate (*6*), which either lets an atom pass through or directs it back. The role of the optical gate may be played by a laser beam. The information may be read from a change in the laser beam phase, while the mechanical action of the gate on an atom may be caused by the dipolar strength of the light pressure of laser beam *6*. In turn, being a measuring instrument, the laser beam inevitably has a back perturbative reaction on the atomic motion (increases the atomic momentum).

To implement this idea, one should find out (1) whether it is possible to gain reliable information from an individual atom and (2) to what extent the back reaction of the laser beam ("read–gate") is destructive; i.e., to what extent it impedes the use of information for the selection of atoms and lowering their temperature.

Let us first make qualitative estimates of the laser phase shift induced by an atom crossing the laser beam. The electric field strength of the laser beam can be represented as

$$E(z, t) = E_0 \exp[i(\omega t - kz)], \tag{1}$$

where ω is the emission frequency, z is the coordinate along the laser beam, and E_0 is the electric field amplitude. The wave number k of an electromagnetic wave interacting with an atom is [9]

$$k^2 = \mu\epsilon(\omega/c)^2, \tag{2}$$

where the dielectric constant ϵ of an atomic medium is expressed through the complex dielectric susceptibility χ and the atomic parameters as follows:

$$\epsilon = 1 + 4\pi\chi, \tag{3}$$

$$\chi = \chi'(\omega) + i\chi''(x) = \frac{N_a|\mu_{12}|^2}{3\epsilon_0\hbar V}\frac{(\omega - \omega_0) + i\gamma}{(\omega - \omega_0)^2 + \gamma^2 + \Omega_R^2}. \tag{4}$$

In Eq. (4), N_a is the number of atoms, V is the volume occupied by the atoms in the laser beam, ω_0 is the frequency of the atomic transition, 2γ is its full width, μ_{12} is the dipole moment matrix element of a two-level atom, and $\Omega_R \equiv \mu_{12}E/2\hbar$ is the Rabi frequency. Then, wave number (2) can be written as

$$k = k_0\left[1 + \frac{\chi'(\omega)}{2}\right] - ik_0\frac{\chi''(\omega)}{2}, \tag{5}$$

where $k_0 = 2\pi/\lambda_0$ and λ_0 is the laser wavelength outside the atomic medium.

The radiation phase shift caused by the atomic medium is equal to (the radiative shift is ignored)

$$\Delta\varphi = k_0\frac{\chi'}{2} = k_0\frac{N_a|\mu_{12}|^2 z}{3\epsilon_0\hbar V}\frac{(\omega - \omega_0)}{(\omega - \omega_0)^2 + \gamma^2 + \Omega_R^2} = \frac{N_a}{V}\sigma(\omega)\frac{(\omega - \omega_0)}{\gamma}z, \tag{6}$$

where σ_0 is the atomic absorption cross section at frequency ω. It follows from Eq. (6) that the laser phase shift is expected to be maximum if the detuning $\delta \equiv (\omega - \omega_0) = \gamma$; the corresponding value is equal to

$$\Delta\varphi_{\max} \cong \frac{1}{2}\frac{\sigma_0}{s}N_a = \frac{1}{4\pi^2}\frac{\lambda^2}{w_0^2}N_a, \tag{7}$$

where s is the laser beam cross section, w_0 is the beam waist radius, σ_0 is the atomic absorption cross section at the exact resonance ($\delta = 0$), and λ is the wavelength. The maximum phase shift per atom is

$$\Delta\varphi_{1,\max} = \frac{1}{4\pi^2}\frac{\lambda^2}{w_0^2} \le \frac{1}{4\pi}\ \text{(rad)}. \tag{8}$$

To understand to what extent phase shift (8) can be informative, one should compare it with the phase quantum noise (the technical noises are assumed to be eliminated):

$$\delta\varphi_n = \frac{1}{\sqrt{n}} = \left(\frac{\hbar\omega}{I_{\text{las}}s\tau_{\text{meas}}}\right)^{1/2}, \tag{9}$$

where n is the number of laser photons detected during the measurement time τ_{meas} and I_{las} is the laser intensity.

Making use of Eqs. (7)–(9), one obtains for the signal-to-quantum noise ratio

$$\frac{S}{N} \equiv \frac{\Delta\varphi_{1,\max}}{\delta\varphi_N} = \left(\frac{1}{8}\frac{\sigma_0}{\pi w_0^2}G\frac{\tau_{\text{meas}}}{\tau_{sp}}\right)^{1/2}, \tag{10}$$

where $G \equiv I_{\text{las}}/I_s$, I_s is the atomic transition saturation intensity and $\tau_{sp} = 1/2\gamma$ is the spontaneous decay time of the excited atomic state. Since the measurement time τ_{meas} is determined by the laser beam diameter and atomic velocity ϑ ($\tau_{\text{meas}} = 2w_0/v$), it follows from Eq. (10) that the signal-to-noise ratio in the course of recording an atom depends on the following three atomic and laser parameters: the saturation parameter G, the atomic velocity v, and the beam diameter $2\omega_0$:

$$S/N \sim (G/v\omega_0)^{1/2}. \tag{11}$$

The increase in the S/N ratio by virtue of a decrease in the beam diameter is limited by the wavelength ($\omega_0 \le \lambda$). The saturation parameter G and the atomic velocity are also not free parameters of the problem because of the diffusive increase in the atomic momentum by the laser field; therein is the manifestation of the back reaction of a meter (laser beam) on the metered object (atom). Let

us analyze this back reaction. The diffusive momentum heating of an atom by laser radiation during the interaction time $t_{\rm int}$ is [10]

$$\langle \Delta p^2 \rangle = 2Dt_{\rm int}, \tag{12}$$

where the momentum diffusivity D of a two-level atom is given by the expression

$$D = \hbar^2 k^2 \gamma G/(1 + G + \delta^2/\gamma^2). \tag{13}$$

The diffusion in momentum space (12) determines the minimum temperature for an atomic ensemble in the laser field [10]:

$$T_{\rm min} = \langle \Delta p^2 \rangle / 2m = \hbar k \gamma, \tag{14}$$

where m *i*s the atomic mass.

Substituting the interaction time $\tau_{\rm int}$ from Eq. (12) for the measurement time $\tau_{\rm meas}$ in Eq. (10), one obtains for the S/N ratio

$$\frac{S}{N} = \left(2\frac{\sigma_0}{\pi\omega_0^2}\frac{T_{\rm min}}{T_{\rm rec}}\right)^{1/2}, \tag{15}$$

where $T_{\rm rec} \equiv \hbar^2 k^2/2mk_B$ is the temperature corresponding to the atomic recoil energy and k_B is the Boltzmann constant. It then follows that the lowest attainable temperature in informational laser cooling is

$$T_{\rm min} = \left(\frac{S}{N}\right)^2\left(\frac{\pi\omega_0^2}{2\sigma_0}\right)T_{\rm rec}. \tag{16}$$

The physical meaning of Eq. (16) is as follows. A sequence of atoms crosses laser beam *4* (see figure). Each atom induces phase shift $\Delta\varphi$, which is measured with an accuracy of S/N. If the S/N ratio is sufficient for gaining information on the atomic motion and selecting this atom (either letting it pass through or directing it back), then the stationary temperature of the selected atoms is equal to $T_{\rm min}$.

The estimation of the lowest attainable atomic temperature in the method of informational cooling gives, for the smallest possible (and hard to realize in practice) laser beam diameter $w_0 = \lambda$ and the signal-to-phase quantum noise ratio $S/N = 3$,

$$T_{\rm min} = 9\pi^2 T_{\rm rec} \gg T_{\rm rec}. \tag{17}$$

Temperature (17) is high enough. At present, varied laser cooling methods [3] allow one to attain temperatures comparable with the recoil temperature $T_{\rm rec}$. As for evaporative cooling [11], the respective temperatures of an atomic ensemble are considerably lower than $T_{\rm rec}$.

The situation can be dramatically improved if the laser field is inside a high-Q cavity. One can readily see that, for a laser field in a cavity, the phase shift per atom is determined by Eq. (7) for the phase shift from N_a atoms, with the only difference that the number of atoms N_a should be replaced by the number N_{ph} of photon passes in the cavity during the mean photon lifetime in the cavity,

$$\Delta\varphi^p_{1,\,\rm max} = \frac{1}{4\pi}\frac{\lambda^2}{w_0^2}N_{ph}. \tag{18}$$

The mean number of photon passes through the cavity is determined by its Q value and may be very long:

$$N_{ph} = \frac{1}{\pi}\frac{\Delta\omega}{\omega}Q = \frac{F}{\pi}, \tag{19}$$

where $\Delta\omega$ is the free spectral range of the cavity and F is its finesse. Then the lowest attainable atomic temperature for the laser beam inside the cavity becomes

$$T_{\rm min} = \left(\frac{S}{N}\right)^2\left(\frac{\pi^3}{2}\frac{w_0^2}{\sigma_0}\right)\frac{1}{F^2}T_{\rm rec}. \tag{20}$$

For a cavity with finesse $F = 10^6$ (commercially available), a laser beam cross section $s = 10^4\sigma_0$, and a signal-to-noise ratio $S/N = 3$, the minimum temperature becomes

$$T_{\rm min} \simeq 10^{-6}T_{\rm rec}, \tag{21}$$

i.e., considerably lower then the recoil temperature.

The above qualitative estimates of the phase shift of an optical wave inside a cavity are confirmed, to a numerical factor, by the exact solution of a coupled system of Maxwell–Bloch equations involving the laser electric field strength, atomic polarization, etc.

A detailed analysis of the atomic selection and formation of a cold atomic ensemble will be carried out elsewhere.

This work was supported by the Russian Foundation for Basic Research (project no. 99-02-16215) and the program "Fundamental Metrology."

REFERENCES

1. Zh. I. Budker, At. Énerg. **22**, 346 (1967).
2. Zh. I. Budker and A. N. Skrinskiĭ, Usp. Fiz. Nauk **124**, 561 (1978) [Sov. Phys. Usp. **21**, 277 (1978)].
3. H. Metcalf and P. van der Straten, *Laser Cooling and Trapping* (Springer-Verlag, New York, 1999).
4. M. H. Anderson, J. R. Ensher, M. R. Matthews, *et al.*, Science (Washington, D.C.) **269**, 198 (1995).
5. J. C. Maxwell, *Theory of Heat* (Longmans, London, 1871).
6. S. van der Meer, Rev. Mod. Phys. **57** (3), 689 (1985).
7. V. I. Balykin, V. G. Minogin, and V. S. Letokhov, Rep. Prog. Phys. (in press, 2000).
8. V. I. Balykin, Adv. At. Mol. Opt. Phys. **41**, 181 (1999).
9. R. Loudon, *The Quantum Theory of Light* (Clarendon, Oxford, 1973).
10. V. S. Letokhov, V. G. Minogin, and V. B. Pavlik, Zh. Éksp. Teor. Fiz. **72**, 1318 (1977) [Sov. Phys. JETP **45**, 698 (1977)].
11. W. Ketterle and N. J. van Druten, Adv. At. Mol. Opt. Phys. **36** (1996).

Translated by V. Sakun

JETP Letters, Vol. 72, No. 1, 2000, pp. 14–17. Translated from Pis'ma v Zhurnal Éksperimental'noĭ i Teoreticheskoĭ Fiziki, Vol. 72, No. 1, 2000, pp. 23–27.

The Antiferromagnetic Photovoltaic Effect

V. V. Men'shenin* and E. A. Turov

Institute of Metal Physics, Ural Division, Russian Academy of Sciences,
ul. S. Kovalevskoi 18, Yekaterinburg, 620219 Russia
**e-mail: menshenin@imp.uran.ru*

Received May 30, 2000

It is established that the photovoltaic effect may occur in centroantisymmetric antiferromagnets. It is due to nontrivial transformations of the antiferromagnetic vector upon atomic transposition under the action of crystallochemical symmetry group elements of a medium. The direction of the photovoltaic current is shown to be governed by the crystal symmetry, its exchange magnetic structure, and the orientation of the antiferromagnetic vector about the crystallographic axes. © *2000 MAIK "Nauka/Interperiodica".*

PACS numbers: 72.15.Gd; 72.20.My; 61.50.Ah

The photovoltaic effect consists in the generation of a direct electric current by light in a medium in the absence of external fields and spatial inhomogeneities [1]. At present, it is studied in detail for nonmagnetic crystals without a symmetry center (SC). The latter is quite significant, because in such systems the detailed balance is not fulfilled for the direct and reverse electron transitions [1, 2]. This alters the kinetic properties of a crystal; in particular, the direction of the photoelectric current is determined only by crystal symmetry [1, 3].

In this work, we predict that the antiferromagnetic photovoltaic effect (AFPE) can be observed in centroantisymmetric (CAS) antiferromagnets (AFs). The occurrence of this effect in such AFs can be understood from the symmetry considerations. When writing the invariant relationships for the material tensors, energy, etc., one should proceed from the crystallochemical spatial symmetry (Fedorov group G_F) if the antiferromagnetic ordering vector parameter **L** (antiferromagnetic vector), which breaks this symmetry, is set off in these relationships in an explicit form [4, 5]. The situation somewhat resembles the magnetophotovoltaic effect ([1, Sect. 1.9]). However, there is a quite important distinction associated with the different transformation properties of the magnetization vector **M** in [1] and the vector **L** in the systems at hand. A case in point is the role of atomic transposition under the action of the group G_F element (along with the rotations and reflections in the point group corresponding to G_F). The transpositions do not affect the **M** vector, whereas the transformation properties of the **L** vector may be substantially altered. Therein lies the basic distinction between the CAS AF considered in this work and the nonmagnetic crystals without SC considered in [1].

Recall in this connection [4, 5] that in media where all magnetic ions occupy the same crystallochemical site, while the G_F group contains SC $\bar{1}$, the symmetry element, depending on the lattice point, can transpose a given magnetic atom either into the same magnetic sublattice (the even symmetry element) or into the sublattice with oppositely directed magnetization (the odd element). In the first case, its action on the **L** vector is no different from the action of the point group element, even if it is a screw axis or glide plane. In the second case (CAS structure), **L** additionally changes sign, in particular,

$$\bar{1}\mathbf{L} = -\mathbf{L}. \tag{1}$$

In the CAS AFs considered below, the pure SC is absent, so that, in accordance with the general rule, the photovoltaic effect is allowed. Accordingly, the density of the direct electric current generated by light can be written as

$$j_i = \beta_{ijkl} L_j e_k e_l^* J \tag{2}$$

(two coinciding indices imply summation over them), where **e** is the unit vector of the monochromatic light wave polarization and J is the light intensity. Clearly, Eq. (2) holds only in CAS AFs for which a change in sign of j_i on the left-hand side under the action of $\bar{1}$ is compensated, according to Eq. (1), by a change in sign of **L** on the right-hand side.

To determine the symmetry properties of the tensor β_{ijkl}, we use the fact that the current density is real: $j = j^*$. Then $\beta_{ijkl} = \beta_{ijlk}^*$, from whence it follows that

$$\begin{aligned} \mathrm{Re}\beta_{ijkl} &= \mathrm{Re}\beta_{ijlk} = \beta_{ijkl}^L, \\ \mathrm{Im}\beta_{ijkl} &= -\mathrm{Im}\beta_{ijlk} = \beta_{ijm}^C \epsilon_{mkl}, \end{aligned} \tag{3}$$

where the β_{ijm}^C tensor does not possess any general properties as regards the permutation of indices and is

only characterized by the symmetry of a medium, and ϵ_{mkl} is the Levi–Civita tensor.

Taking into account Eq. (3), Eq. (2) can be recast in the form

$$j_i = (\beta^L_{ijkl} e_k e_l^* + i\beta^C_{ijm}[ee^*]_m) L_j J. \quad (4)$$

The second term in Eq. (4) is nonzero only for the complex polarization vector, i.e., for elliptically polarized light, while the first term

$$j_i^L = \beta^L_{ijkl} e_k e_l^* L_j J = \frac{1}{2}\beta^L_{ijkl}(e_k e_l^* + e_k^* e_l) L_j J \quad (5)$$

is nonzero for both elliptical and linear polarizations, when $\mathbf{e} = \mathbf{e}^*$. In the latter case, let us call current (5) the linear antiferromagnetic photovoltaic current, which will only be considered in what follows. In this situation, Eq. (5) takes the form

$$j_i^L = \beta^L_{ijkl} e_k e_l L_j J. \quad (6)$$

The β^L_{ijkl} tensor is symmetric about the permutation of the last two indices. One can readily show that, symmetrically, β^L_{ijkl} coincides with the piezomagnetic tensor whose explicit form is given in [6] for different space groups.

Let us consider some particular AFs where this effect can be observed. For this purpose, we first call attention to the fact that the photovoltaic effect in nonmagnetic crystals was observed in high-energy-gap semiconductors, piezoelectric materials, and ferroelectrics, where the intrinsic conductivity is small. One can thus assume that the AFPE can be observed in nonconducting CAS antiferromagnetic crystals. One of such AFs is Cr_2O_3. Its crystallochemical space group is $R\bar{3}c = D^6_{3d}$), the Neél temperature $T_N = 318$ K, the exchange magnetic structure (EMS) (mutual orientation of the sublattice magnetizations) is coded as $\bar{1}(-)3_z(+)2_x(-)$, and the orientation state is $-\mathbf{L} \parallel \mathbf{z}$. The signs "+" and "–" in the code stand for the even and odd symmetry elements, respectively.

CAS AFs are also present among crystals of the tetragonal system. These are trirutiles (space group $P4_2/mnm = D^{16}_{4h}$), e.g., Fe_2TeO_6 ($T_N = 219$ K) with EMS $\bar{1}(-)4_z(+)2_d(-)$ and $\mathbf{L} \parallel \mathbf{z}$ (easy axis); Cr_2TeO_6 ($T_N = 105$ K) with EMS $\bar{1}(-)4_z(+)2_d(-)$ and $\mathbf{L} \perp \mathbf{z}$; and Cr_2WO_6 ($T_N = 69$ K) and V_2WO_6 ($T_N = 370$ K) with vector $\mathbf{L} \perp \mathbf{z}$ and EMS $\bar{1}(-)4_z(-)2_d(-)$; and rare-earth orthophosphates and orthovanadates of the $DyPO_4$ ($T_N = 3.4$ K) and $CdVO_4$ ($T_N = 2.4$ K) types (space group $I4_2/amd = D^{19}_{4h}$) with EMS $\bar{1}(-)4_z(-)2_d(\mp)$ and $\mathbf{L} \parallel \mathbf{z}$.

Let us now offer some examples of linear AFPE that can be experimentally verified in structures even about the principal symmetry axis:

A. EMS $\bar{1}(-)3_z(+)2_x(+)$ and $\bar{1}(-)3_z(+)2_x(-)$.

Note, first of all, that the structures with the even and odd 2_x axis can be easily distinguished by the photovoltaic effect if the antiferromagnetic axis $\mathbf{L}$ is oriented along the 3_z axis and the light is also polarized along this axis, so that $\mathbf{e} = \{0, 0, 1\}$. The light propagation direction ($\mathbf{k} \parallel \mathbf{x}$ or $\mathbf{k} \parallel \mathbf{y}$) is immaterial in this case. One then has

$$\begin{aligned} &2_x(+) && 2_x(-) \\ &j = \{0, 0 j_z\}, \quad && j = 0, \\ &j_z = \beta_1^{(+)} L_z J. \end{aligned} \quad (7)$$

In Eq. (7), $\beta_1^{(+)} = \beta^L_{3333}$ is the photovoltaic constant. Therefore, in this situation the linear photovoltaic current is absent in the structures with $2_x(-)$, whereas in the system with the $2_x(+)$ axis the current is induced along the antiferromagnetic vector.

Let us next consider the easy-axis AF with $\mathbf{L} \parallel \mathbf{3}_z$ and the light polarization $\mathbf{e} = \{\cos\varphi, \sin\varphi, 0\}$. For this polarization, the photocurrent is

$$\begin{aligned} &2_x(+) && 2_x(-) \\ &j_x = \beta_2^{(+)} \sin 2\varphi L_z J, \quad && j_x = \beta_1^{(-)} \cos 2\varphi L_z J, \\ &j_y = \beta_2^{(+)} \cos 2\varphi L_z J, \quad && j_y = -\beta_1^{(-)} \sin 2\varphi L_z J, \\ &j_z = \beta_3^{(+)} L_z J, && j_z = 0, \end{aligned} \quad (8)$$

where, again, $\beta_{2,3}^{(+)}$ and $\beta_1^{(-)}$ are the photovoltaic constants. It follows from Eqs. (8) that, in the media with symmetry axis $2_x(-)$, the photocurrent along the z axis is also absent for the indicated light polarization. An analysis of the limiting cases of light polarization along the x or y axis shows that the photocurrent directions in the media with $2_x(+)$ and $2_x(-)$ are mutually perpendicular. In the media with $2_x(-)$, the photocurrent flows precisely along (or opposite) this symmetry axis for both polarization directions.

In AFs of the easy-plane type, one has, for the same EMS, $\mathbf{L} \parallel \mathbf{x}$, and light polarization as above,

$$\begin{aligned} &2_x(+) \\ &j_x = L_x(\beta_4^{(+)} \cos^2\varphi + \beta_5^{(+)} \sin^2\varphi) J, \\ &j_y = (\beta_4^{(+)} - \beta_5^{(+)}) L_x \sin 2\varphi J/2, \\ &j_z = \beta_6^{(+)} L_x \sin 2\varphi J, \\ &2_x(-) \\ &j_x = (\beta_2^{(-)} - \beta_3^{(-)}) L_x \sin 2\varphi J/2, \\ &j_y = -L_x(\beta_2^{(-)} \cos^2\varphi + \beta_3^{(-)} \sin^2\varphi) J, \\ &j_z = \beta_4^{(-)} L_x \cos 2\varphi J. \end{aligned} \quad (9)$$

It is seen from Eqs. (9) that, in the easy-plane crystals with the $2_x(+)$ axis, the **z** component of the photocurrent is zero in the limiting situations of light polarization along the *x* or *y* axis and only the *x* component is nonzero.

Let us now turn to the tetragonal AFs in which the principal axis 4_z is either an even or odd symmetry element. Among these are Fe_2TeO_6, Cr_2TeO_6 and Cr_2WO_6, V_2WO_6:

$$\text{B. EMS } \bar{1}(-)4_z(+)2_d(-), \quad \bar{1}(-)4_z(-)2_d(-),$$

respectively. Let us first consider the AFs with **L** || **z**. An analysis of the AFPE shows that for light polarized along the *z* axis the photocurrent is absent, irrespective of the parity of the 4_z axis. For the light polarization $\mathbf{e} = \{\cos\varphi, \sin\varphi, 0\}$, the current density is

$$\begin{array}{cc} 4_z(+) & 4_z(-) \\ j = 0. & j_x = 0,\ j_y = 0, \\ & j_z = \beta_1^{(-)T}\cos 2\varphi L_z J. \end{array} \tag{10}$$

One can see that AFs differing in the parity of the 4_z axis differ substantially for this light polarization: for the $4_z(+)$ axis, the current is completely absent, whereas in AFs with the $4_z(-)$ axis, the current can flow only along the **z** direction.

In AFs of the easy-plane type with the above-mentioned EMS, the orientation $\mathbf{L} = (L\cos\Omega, L\sin\Omega, 0)$, and the light polarization $\mathbf{e} = \{0, \cos\varphi, \sin\varphi\}$, the photovoltaic current components are

$$\begin{gathered} 4_z(+) \\ j_x = L\sin\Omega(\beta_2^{(+)T}\cos^2\varphi + \beta_3^{(+)T}\sin^2\varphi)J, \\ j_y = -L\cos\Omega(\beta_1^{(+)T}\cos^2\varphi + \beta_3^{(+)T}\sin^2\varphi)J, \\ j_z = \beta_4^{(+)T}L\cos\Omega\sin 2\varphi\frac{J}{2}, \\ 4_z(-) \\ j_x = L\cos\Omega(\beta_2^{(-)T}\cos^2\varphi + \beta_3^{(-)T}\sin^2\varphi)J, \\ j_y = -L\sin\Omega(\beta_4^{(-)T}\cos^2\varphi + \beta_3^{(-)T}\sin^2\varphi)J, \\ j_z = -\beta_5^{(-)T}L\sin\Omega\sin 2\varphi\frac{J}{2}. \end{gathered} \tag{11}$$

It follows from Eq. (11) that in the limiting cases of **L** orientation along the **x** or **y** coordinate axis, the currents in AFs with EMSs even or odd about the 4_z axis are mutually perpendicular. Note that the photocurrents are also mutually perpendicular for the above-mentioned **L** directions and the same parity of the 4_z axis. In this case, for AFs with the EMS odd about the 4_z axis and with **L** || **x**, the current flows along the **x** axis, while for **L** || **y**, it has nonzero j_y and j_z components. In the even case, the current components obey the reverse relationship. It is also worth noting that, for the **x**-oriented vector **L**, the j_z component of the photocurrent is present only in the structures even about the 4_z axis, whereas for **L** || **y**, it only occurs in the systems with the $\bar{1}(-)4_z(-)2_d(-)$ EMS.

Let now consider orthophosphates and orthovanadates, whose EMSs have the same parity about the principal symmetry axis but different parities of the twofold axes:

$$\text{C. EMS } \bar{1}(-)4_z(-)2_d(-), \quad \bar{1}(-)4_z(-)2_d(+).$$

In AFs of the easy-axis type, the photocurrent does not arise for the light polarized along the **z** axis, irrespective of the parity of the 2_d axis.

For the light polarization $\mathbf{e} = \{\cos\varphi, \sin\varphi, 0\}$ in the direction perpendicular to **L**, one has for the photocurrent density in an AF with the even 2_d axis

$$j_x = 0, \quad j_y = 0, \quad j_z = \beta_1^{(-)'}\sin 2\varphi L_z J/2. \tag{12}$$

One can see from the comparison of Eqs. (11) and (12) that, for this light polarization, the current is an odd function of the angle φ for the even 2_d axis and vice versa, although its components are the same as above. In the situation where the light is polarized along the coordinate axes ($\varphi = 0$ or $\pi/2$), the photocurrent is absent in media with the even 2_d axis but arises in systems with the $2_d(-)$ axis. If the light is polarized as $\mathbf{e} = \{0, \cos\varphi, \sin\varphi\}$ or $\mathbf{e} = \{\cos\varphi, 0, \sin\varphi\}$, then the photocurrents in the indicated AFs are mutually perpendicular.

For AFs of the easy-axis type with the principal $4_z(-)$ axis and the even twofold axis, we consider the case where $\mathbf{L} = (L\cos\Omega, L\sin\Omega, 0)$ and the light polarization is $\mathbf{e} = \{0, \cos\varphi, \sin\varphi\}$. Then the photocurrent density can be written as

$$\begin{gathered} j_x = L\sin\Omega(\beta_2^{(-)'}\cos^2\varphi + \beta_3^{(-)'}\sin^2\varphi)J, \\ j_y = L\cos\Omega(\beta_4^{(-)'}\cos^2\varphi + \beta_3^{(-)'}\sin^2\varphi)J, \\ j_z = \beta_5^{(-)'}L\cos\Omega\sin 2\varphi J/2. \end{gathered} \tag{13}$$

In this situation, crystals with the even and odd 2_d axes can easily be distinguished by the current direction as a function of the orientation of vector **L**.

Thus, the AFPE in AFs is influenced not only by the crystallochemical symmetry but by the magnetic state of the crystal as well. For instance, depending on the EMS and orientation of vector **L**, the photocurrent directions in crystals with the same crystallochemical symmetry can be substantially different, as, e.g., it follows from Eqs. (8), (9), (11), and (13); moreover, the photocurrent may be nonzero in one crystal and completely absent in the other.

The formulas presented above are derived for a single-domain sample. However, it is clear that the AFPE may disappear in a multidomain sample merely because the current direction changes upon changing the direction of vector **L**. For this reason, it should be borne in mind that, e.g., 180° and 90° domains can exist in easy-plane tetragonal AFs. To eliminate these domains and make the sample single-domain, it is necessary to anneal it in crossed magnetic and electric fields, because the magnetoelectric interaction will bring the system to the most energetically favorable state with uniform orientation of **L** throughout the crystal, while the magnetic field will suppress the 90° domains.

This work was supported by the Russian Foundation for Basic Research, project no. 99-02-16268.

REFERENCES

1. B. I. Sturman and V. M. Fridkin, *Photovoltaic Effect* (Nauka, Moscow, 1992).
2. A. S. Davydov, *Quantum Mechanics* (Nauka, Moscow, 1973).
3. V. I. Belinicher and B. I. Sturman, Usp. Fiz. Nauk **130**, 415 (1980) [Sov. Phys. Usp. **23**, 199 (1980)].
4. E. A. Turov, *Kinetic, Optical, and Acoustic Properties of Antiferromagnets* (Sverdlovsk, 1990).
5. E. A. Turov, Usp. Fiz. Nauk **164**, 325 (1994) [Phys. Usp. **37**, 303 (1994)].
6. A. I. Mitsek and V. G. Shavrov, Fiz. Tverd. Tela (Leningrad) **6**, 210 (1964) [Sov. Phys. Solid State **6**, 167 (1964)].

Translated by V. Sakun

JETP Letters, Vol. 72, No. 1, 2000, pp. 18–20. Translated from Pis'ma v Zhurnal Éksperimental'noĭ i Teoreticheskoĭ Fiziki, Vol. 72, No. 1, 2000, pp. 28–32.

Anomalous Compressibility and Magnetostriction of Beryllium under the Conditions of Diamagnetic Domain Formation

V. S. Egorov*, F. V. Lykov, and O. A. Repina

Russian Research Centre Kurchatov Institute, pl. Kurchatova 1, Moscow, 123182 Russia
**e-mail: egorov@isssph.kiae.ru*

Received May 31, 2000

Magnetostriction oscillations are measured for a single-crystal beryllium sample shaped like a plate perpendicular to the direction of the magnetic field. In the range of 2–5 T at a temperature of 1.5 K, i.e., in the region of diamagnetic domain formation (Condon domains), the striction signal has the saw-tooth shape corresponding to the alternation of homogeneous and nonhomogeneous (domain) states. The formation of the domain structure is accompanied by an anomalous increase in compressibility; the oscillations in this coefficient are more than one hundred times greater than the value given by the standard theory. An analysis of the results indicates that the domain wall width should increase with increasing plate thickness. © *2000 MAIK "Nauka/Interperiodica".*

PACS numbers: 75.80.+q; 75.60.Ch; 62.20.Dc

Chandrasekhar was the first to suggest in 1963 that magnetization oscillations—the de Haas–van Alphen (dHvA) effect—should be accompanied by oscillations in magnetostriction. Within the next few years, magnetostriction oscillations were experimentally observed in Ag, As, Bi, Cd, Cu, Ga, Sb, Sn, and Zn samples [2]. The experiments were also carried out for beryllium samples of different orientations [3]. Both in [3] and in all other cases, the demagnetization factor of the samples, as a rule, was much smaller than unity, which is typical of the experiments on the dHvA effect. Because of this, no diamagnetic domains were formed in the samples.

It was the purpose of this work to study striction in the presence of diamagnetic domains [4], i.e., in the situation where, first,

$$-\frac{\partial^2\tilde{\Omega}}{\partial B^2} = \frac{\partial M}{\partial B} > \frac{1}{4\pi} \qquad (1)$$

($\tilde{\Omega}$ is the oscillating part of the electron gas energy, B is the magnetic flux density in the sample, and M is the magnetization) and, second, the demagnetization factor in the direction of external magnetic field is close to unity.

Insofar as the oscillation period δB is proportional to B^2, so that it increases faster than the amplitude $M(B)$, Eq. (1) imposes an upper bound on the range of magnetic fields where the domains are formed. At the same time, the spacing between the Landau levels should be appreciably greater than the temperature; i.e., $\hbar\omega \gg kT$, so that rather low temperatures are required. Moreover, the magnetic field should be strong enough for this spacing to be greater than the width $\hbar/\tau$ of the Landau level; in other words, the condition $\omega\tau > 1$ should be fulfilled. Here, ω is the cyclotron frequency of conduction electrons in the field and τ is the electron mean free time in the sample. Thus, the lower bound of the indicated field range is determined not only by the temperature but also by the sample quality. Within this range, the domains periodically arise in the sample, the magnetization vector in each of them being either aligned or antialigned with the external magnetic field.

The formation of Condon domains was previously observed in beryllium, e.g., while investigating the magnetic breakdown oscillations for the thermoelectromotive force and resistance and in muon-spin resonance (μSR) measurements at temperatures of 0.8–4.2 K in magnetic fields as high as 3 T [5, 6]. These measurements have demonstrated the formation of a diamagnetic domain structure at $T \leq 3$ K in the sample studied. We carried out measurements of size oscillations for the same beryllium single crystal under the conditions of diamagnetic domain formation.

A platelike beryllium single crystal of size $11 \times 9 \times 1.8$ mm was cut in such a way that the hexagonal crystallographic axis was directed along the short edge. The ratio of resistivities at room temperature and liquid helium was $\rho_{300}/\rho_{4.2} \approx 300$. Measurements were carried out for the oscillations of sample size $\delta l \equiv \epsilon l$ along the long edge. To this end, the sample was placed in a dilatometer (Fig. 1) operating on the principle of measuring the capacitance of a plane capacitor. Since the working face of the sample was small, one could hardly use it as a moving capacitor plate, as is customarily done, e.g., in [7]. Because of this, the moving plate was made in the form of a separate spring-loaded plate with

a sharpened bulge that leaned upon the sample. The opposite face leaned against the adjusting screw, which could slightly move the sample and adjust the separation between the capacitor plates to the position in which the capacitance corresponded to the highest resolution of the bridge. The sample in the dilatometer was placed in the center of a superconducting solenoid. The magnetic field was parallel to the hexagonal axis of the sample and, correspondingly, perpendicular to the plate plane. It is worth noting that the same sample in the same solenoid was used at the same temperatures in [5] for observation of magnetic breakdown oscillations in the resistance and thermoelectromotive force. In that work, the character of the field dependence of these oscillations was indicative of the formation of diamagnetic domains. This gave us grounds to assume that, despite the lack of additional control, diamagnetic domains were formed during our measurements in the same magnetic-field and temperature ranges as well.

Measurements were made using a TESLA BM484 semiautomated bridge in both liquid helium (normal or superfluid) and its vapor. The results tangibly differed both in the noise level and in character. The most suitable situation for the measurements occurred when the dilatometer was over the helium level. At 1.5 K, the noise was equal to $\sim 0.5 \times 10^{-3}$ pF; for a capacitance of ~100 pF and, correspondingly, a capacitor gap of $\sim 10^{-3}$ cm, this corresponded to the relative deformation of the sample $\epsilon \equiv \delta l/l \sim 5 \times 10^{-9}$.

The magnetostriction measurements were carried out in magnetic fields from 10 to 70 kOe at helium temperatures. The most demonstrative results are presented in Fig. 2. The magnetic-field dependence of striction at $T = 4.2$ K and in low fields agrees well with the results obtained earlier in [3]. These curves have the usual shape and are almost identical to the magnetic moment oscillations with beats typical of beryllium (Fig. 2a). However, at a temperature of 1.5 K and in fields from 25 to 55 kOe, i.e., under the conditions and in the field range where the diamagnetic domains are formed in the sample, the signal pattern becomes much more complicated. Namely, starting at $H \sim 25$ kOe, small dips appear in the amplitude near the size maxima (Fig. 2b), so that double maxima are clearly seen. As the magnetic field increases, the depth of these dips also increases. In the range from 39 to 42 kOe, the dips become comparable with the striction as if the oscillation frequency were doubled (Fig. 2c). On further field build-up, the oscillations assume the usual shape of magnetic moment oscillations.

We assumed that this anomaly was caused by two factors: the formation of domains and local inhomogeneous deformation under the tip. The same measurements were repeated with copper spacers under the tips. As a result, the "usual" features remained virtually unchanged, while the anomalous behavior fully disappeared. In the domain range, the signal has the sawtooth shape and its amplitude sizably increases (Fig. 2d). This

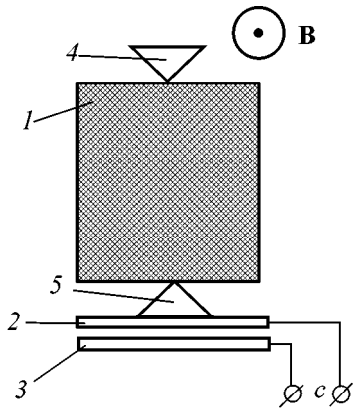

Fig. 1. Schematic representation of the sample in the dilatometer: *1* is a beryllium single crystal; the magnetic field and the hexagonal axis of the sample are perpendicular to the drawing plane; *2* is the moving spring-loaded capacitor plate; *3* is the fixed capacitor plate; *4* is the adjusting screw tip; *5* is the bulge at the moving plate; and *C* is the measured capacitance.

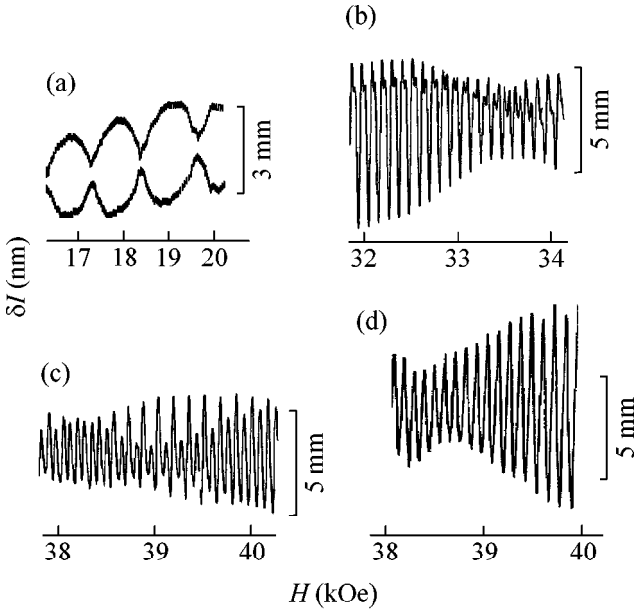

Fig. 2. Sample size oscillations in a magnetic field at $T = 1.5$ K: (a)–(c) obtained using the measuring scheme illustrated in Fig. 1; (a) the high oscillation frequency is not seen, and only the envelope from peak to peak is shown; (d) with spacers under the tips. The scale is shown to the right of each curve.

implies that, apart from the usual striction $\delta l = \epsilon l$, one should, in principle, take into account an additional oscillating deformation

$$\delta l' = \tilde{h}_0 + \tilde{h} \qquad (2)$$

caused by the load (though small) and the compressibility oscillations. In Eq. (2), h_0 is the static homogeneous deformation under a uniformly distributed load,

h is the deflection depth ("dimple") at the area of crystal surface under the copper tip, and $\tilde{h}_0 + \tilde{h}$ is the oscillatory contribution of these deformations. It is proportional to the compressibility oscillation amplitude and is phase shifted by $\pi/2$ about the striction oscillations. The calculated deflection depth (an analogous problem is solved in [8]) $h \sim 1.5 \times 10^{-5}$ cm and $h_0 \sim 2 \times 10^{-6}$ cm (for a load of ~10 N). In the absence of domains, this oscillatory contribution to the measured signal is ~1% (harmonic approximation) and is not seen. In the presence of a domain structure, i.e., a mixture of two phases with different densities, the compressibility increases. As a result, the tip periodically "collapses" into the sample. (Note that beryllium is one of the hardest metals). If one assumes that the oscillations in dimple depth and the striction are of the same order of magnitude at $H \sim$ 40 kOe (Fig. 2c), then the above estimates imply that the oscillations in the compressibility coefficient increase by ~100 times. With the spacers, the load is uniformly distributed and in this case the oscillations are $\delta l' \sim \tilde{h}_0 \sim 10^{-1}\delta l$ and also phase shifted by $\pi/2$ about ϵ. One can, in principle, observe this contribution at high loads, but in our case it is practically undetectable.

There is no doubt that in a homogeneous phase, be it dia- or paramagnetic, the deformation is isotropic in the basal plane. The deformation can also be considered as isotropic in the presence of the domains of a "new" phase, as long as this new phase is present in a very small amount such that it consists, most probably, of individual inclusions. However, as the volume of the new phase increases, the transition to the energetically more favorable lamellar structure should "rapidly" occur. This is clearly seen from the behavior of the "domains" in the intermediate state of type I superconductors [9], where separate filamentary inclusions exist only in the vicinity of the transition to the normal state.

One cannot confidently state that each phase in the lamellar structure is locally isotropic. Should this be the case, then the difference in the deformations of the neighboring domains would be "accumulated" along the interface, leading to shear stresses and energy increase. Needless to say, it is much more profitable to realize the indicated deformation difference only via the deformation normal to the interface. This would give rise to anisotropic deformation in the domains, although, if there were no preferred direction, then the situation would remain, on average, isotropic for the whole crystal because of the mosaic character of the orientations of the individual lamellar inclusions, as is observed in an analogous situation for the intermediate state of type I superconductors [9]. This scenario seems to be quite realistic also, because it permits one to explain, in part, the observed giant increase in the compressibility upon the formation of the domain structure. The local anomalous deformation under the tip can occur only due to the reorientation and rearrangement of the anisotropic domains.

In any case, the difference in the deformations of the neighboring domains persists in the direction of the magnetic field. This fact forces us to draw the conclusion that the domain wall "width" should increase with increasing crystal thickness. This conclusion is at variance with the commonly accepted assumption that the domain wall width is on the order of the Larmor radius [10].

We are grateful to E.P. Krasnoperov and S.V. Varyukhin for discussion of the results. This work was supported by the Russian Foundation for Basic Research, project no. 98-02-17142.

REFERENCES

1. B. S. Chandrasekhar, Phys. Lett. **6**, 27 (1963).
2. T. E. Thomson, P. R. Aron, B. S. Chandrasekhar, *et al.*, Phys. Rev. B **4**, 518 (1971).
3. B. S. Chandrasekhar, E. Fawcett, D. M. Sparlin, and G. K. White, in *Proceedings of LT10* (VINITI, Moscow, 1967), Vol. 3, p. 328.
4. D. Shoenberg, *Magnetic Oscillations in Metals* (Cambridge Univ. Press, Cambridge, 1984; Mir, Moscow, 1986).
5. V. S. Egorov, E. P. Krasnoperov, F. V. Lykov, *et al.*, Fiz. Tverd. Tela (St. Petersburg) **40**, 524 (1998) [Phys. Solid State **40**, 482 (1998)].
6. G. Solt, C. Baines, V. S. Egorov, *et al.*, Phys. Rev. Lett. **76**, 2575 (1996).
7. G. K. White, Cryogenics **1**, 151 (1961).
8. L. D. Landau and E. M. Lifshitz, *Course of Theoretical Physics*, Vol. 7: *Theory of Elasticity* (Nauka, Moscow, 1965; Pergamon, New York, 1986).
9. T. E. Faber, Proc. R. Soc. London, Ser. A **248**, 460 (1958).
10. A. A. Abrikosov, *Fundamentals of Metal Theory* (Nauka, Moscow, 1987; North-Holland, Amsterdam, 1988).

Translated by V. Sakun

JETP Letters, Vol. 72, No. 1, 2000, pp. 21–25. Translated from Pis'ma v Zhurnal Éksperimental'noĭ i Teoreticheskoĭ Fiziki, Vol. 72, No. 1, 2000, pp. 33–38.

Temperature Dependence of the Upper Critical Field as an Indicator of Boson Effects in Superconductivity in $Nd_{2-x}Ce_xCuO_{4-y}$

V. F. Gantmakher*, G. A. Emel'chenko, I. G. Naumenko, and G. É. Tsydynzhapov

Institute of Solid-State Physics, Russian Academy of Sciences, Chernogolovka, Moscow region, 142432 Russia
**e-mail: gantm@issp.ac.ru*

Received June 1, 2000

The temperature dependence of the upper critical field B_{c2} was determined from the shift of the resistive transition $\Delta T(B)$ in nearly optimally doped $Nd_{2-x}Ce_xCuO_{4-y}$ single crystals. Within the experimental accuracy, the weak-field data are described by the power function $B_{c2} \propto (\Delta T)^{3/2}$. This result is compared with the data on heat capacity and analyzed in the context of possible manifestations of boson effects in superconductivity. The T dependence of B_{c2} persists down to the lowest temperatures, but the numerical values of B_{c2} below 1 K are different for different samples. © *2000 MAIK "Nauka/Interperiodica".*

PACS numbers: 74.20.Mn; 74.25.Dw; 74.72.-h

There are grounds to believe that high-temperature superconductivity (HTSC) is not described by the BCS theory. One of them consists in the relationship between the density n of Cooper pairs and the coherence length ξ (the pair size). In HTSC cuprates, superconductivity is due to the carriers in the CuO_2 plane. As in all 2D systems, the density of states g_F at the Fermi level in the CuO_2 plane does not depend on the carrier concentration in the normal state and, according to measurements, is equal to $g_F = 2.5 \times 10^{-4}$ K^{-1} per structural unit of CuO_2 (this value is nearly the same for all cuprate families, see, e.g., [1], Ch. 13). Assuming that the superconducting gap Δ is on the order of the transition temperature T_c, one estimates the mean distance $r = n^{-1/2} \approx (g_F\Delta)^{-1/2}$ between the pairs in the CuO_2 plane at 25 Å for $T_c \approx 100$ K and 75 Å for $T_c \approx 10$ K. These r values should be compared with the typical coherence length $\xi \approx 20$ Å in the *ab* plane [1], so that $r \gtrsim \xi$ in HTSC materials. Inasmuch as the BCS theory introduces Cooper pairs to describe the Fermi-liquid ground state as a whole, its validity for the description of HTSC is not obvious. This causes interest in the models of superconductivity considering the boson limit $r \gg \xi$ and based on Bose–Einstein condensation (BEC) in a system of charged bosons [2–4]. The experimental evidences for the boson effects in HTSC are presently being intensively accumulated.

One such piece of evidence can be expected from the measurements of the temperature dependence of the magnetic field B_{c2}, which destroys superconductivity. In the BCS theory, the $B_{c2}(T/T_c)/B_{c2}(0)$ function is linear in the vicinity of $T/T_c = 1$; it monotonically increases to saturation near the zero temperature and almost coincides with the limiting value even at $T/T_c = 0.2$ [5]. However, in most cases, HTSC materials behave in a different manner and have a positive second derivative $\partial^2 B_{c2}/\partial T^2$ over the entire temperature range.

The $B_{c2}(T)$ measurements are mainly based on an analysis of the resistive transition. Two types of behavior are known for the resistive transition of HTSC materials in a magnetic field. For one of them, the transition is sizably broadened in a magnetic field, so that it is hard, or even practically impossible, to gain any information about the $B_{c2}(T)$ dependence from it. The other transition is shifted in a magnetic field to lower temperatures and either remains undistorted, as in usual superconductors, or undergoes an insignificant distortion. This usually occurs for those members of HTSC families for which $T_c \lesssim 20$ K. The transition shift in these materials is naturally explained by the field-induced destruction of superconductivity. Irrespective of the mechanism of dissipative processes in the superconducting state, the spectrum rearrangement and the appearance of superconducting pairing should necessarily affect the $R(T)$ resistance. With this proposition, one can readily construct the $B_{c2}(T)$ function.

In almost all HTSC cuprates, such as the Tl-based [6] and Bi-based [7] families and the LaSrCuO [8] and Nd(Sm)CeCuO [9–11] families, as well as in the Zn-doped [12] or oxygen-deficient [13] YBaCuO, the $B_{c2}(T)$ function derived from the shift of the resistive transition has a positive second derivative over the whole temperature range $0 < T/T_c < 1$ and shows a tendency to diverge at small T/T_c values. Most discussions of the $B_{c2}(T)$ curves concentrated precisely on this divergence and considered it as the most dramatic

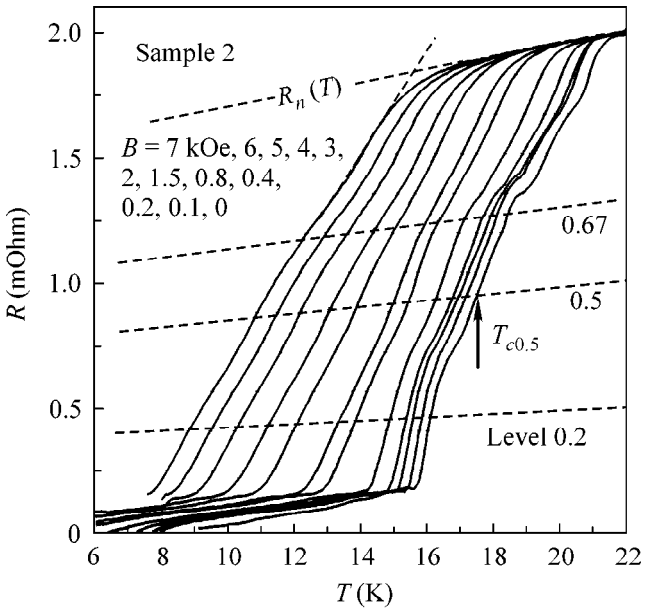

Fig. 1. The $R(T)$ curves for sample 2 in magnetic fields (from right to left) from 0 to 7 kOe. The dashed lines are the straight line $R_n(T)$ and the straight lines at the levels of 0.67, 0.5, and 0.2 of $R_n(T)$. The method of determining the onset of the transition is demonstrated, and the T_{ci} fields from which the shifts were measured are shown.

departure from the BCS theory. At the same time, the behavior of the $B_{c2}(T)$ function near T_c is also quite informative. Contrary to expectations, in almost all cases where the field-induced resistive-transition shift in HTSC cuprates proceeds in a parallel manner, the experimental data indicate that the $\partial B_{c2}/\partial T$ derivative is zero at the T_c point [6–13].

The $\partial B_c/\partial T$ derivative of the critical field at the T_c point is related to the free energy F and heat capacity C at this point by the well-known Rutgers formula:

$$\frac{1}{4\pi}\left(\frac{\partial B_c}{\partial T}\right)^2_{T_c} = \frac{\partial^2}{\partial T^2}(F_s - F_n) = \frac{C_s - C_n}{T_c}. \qquad (1)$$

Inasmuch as the thermodynamic critical field B_c is different from the upper critical field B_{c2}, Eq. (1) can be used only for qualitative estimates. However, being based on thermodynamics, this equation is very useful.

In usual superconductors, $F_s - F_n \propto (T_c - T)^2$, so that the heat capacity undergoes a jump and B_c is linear in $(T_c - T)$. In the BEC case, $F_s - F_n \propto (T_c - T)^3$ and the heat capacity is a continuous function at the transition point [14]. It then immediately follows that $\partial B_c/\partial T = 0$ and

$$B_c \propto (T_c - T)^{3/2}. \qquad (2)$$

Of course, one can hardly imagine that a Fermi gas suddenly and completely transforms into a Bose gas at low temperatures. It was assumed in [4] that bosons appear in small pockets of the k space near the Fermi level. In the isotropic model, one can only speak about pairing of sufficiently energetic fermions, as in the BCS theory. Nevertheless, Eq. (2) deserves serious experimental verification. Such was the motivation of our work consisting in the measurement and analysis of the field-induced shift of the resistive transition in $Nd_{2-x}Ce_xCuO_{4-y}$ single crystals. We will discuss separately the behavior of the B_{c2} field in the vicinity of T_c and at low temperatures.

Experiment. $(NdCe)_2CuO_4$ single crystals were grown from a mixture of components taken in the molar ratio $Nd_2O_3 : CeO_2 : CuO = 1 : 0.05 : 11$ in a crucible made from yttrium-stabilized zirconium dioxide. The use of a modified growth regime markedly reduced the time of interaction between the melt and the crucible at high temperatures. Owing to the accelerated–decelerated crucible rotation, the melt was intensively stirred so that the homogenization time for the molten solution did not exceed 1 h at a temperature near 1150°C. The growth was carried out for several hours upon slow cooling (6 K/h) under the conditions of a morphologically stable crystallization front ($dT/dx \geq 10$ K/cm), after which the crucible was decanted and cooled at a rate of 30–50 K/h to the ambient temperature. The crystals were shaped like platelets 20–40 μm thick. Their composition—$Nd_{1.82}Ce_{0.18}CuO_x$—was determined by local X-ray spectroscopic analysis. The analysis revealed Zn traces in the crystals at a level of 0.1 wt %. Initially, the crystals did not show a superconducting transition above 4.2 K. The superconducting transition at $T_c \approx 20$ K appeared after 15 h of annealing at 900°C in an argon atmosphere.

Measurements were made for two plates approximately 1×2 mm in size. The silver paste contacts were fused in air at a temperature of ~350°C. Four contacts in sample 1 were arranged ~0.5 mm apart in a row on one side of the plate. The potential contacts in sample 2 were placed on the opposite side of the plate beneath the current contacts, allowing the measuring current to be directed both along and transverse to the *ab* plane. This did not affect the results. The resistance was measured by the standard method using a lock-in nanovoltmeter at a frequency of 13 Hz. The measuring current was small enough to provide the linear regime and the absence of overheating down to the lowest temperatures. The magnetic field was directed along the normal to the plate (c axis). Measurements were performed over the temperature range from 25 K to 25 mK.[1] The onset of the zero-field superconducting transition in both samples occurred at about 20.5 K.

The measurements gave identical results for both samples. Figure 1 demonstrates a series of low-field $R(T)$ curves for sample 2. At high temperatures, all curves show the same asymptotic behavior $R_n(T)$ above the transition, and one can assume that the R_n function does not depend on B at $T > 10$–12 K. The zero-field

[1] The low-temperature measurements in strong magnetic fields were carried out at the NHMFL (Tallahassee, Fla., USA).

transition shows a certain structure, which, however, is smoothed out even at 100–200 Oe. The field effect mainly amounts to shifting the transition to lower temperatures. The degree to which this shift is parallel can be checked by comparing the shift of the onset of the transition with the shifts of the $R(T)$ function at different levels: $0.2R_n$, $0.5R_n$, and $0.67R_n$ (see curves in Fig. 1). For the parallel shift, all constructions in Fig. 1 should give the same function $B_{c2}(\Delta T)$, where $\Delta T = T_{ci} - T$ and T_{ci} is the temperature corresponding to the same level on the initial curve $R(T, B = 0)$. The log–log plots of the shifts are shown by different symbols in Fig. 2a for all four levels. The systematic deviations of the symbols from the straight line

$$B_{c2} = (\Delta T)^{\beta} \qquad (3)$$

constructed by averaging the results for all points are small for each of the symbols. This implies that the distortions of the transition shape are small compared to its shift. The scatter of points in low fields is mainly caused by the fine structure of the $R(T, B = 0)$ curve, which serves as a reference in the determination of the shift ΔT. The coefficient β was determined from the slope of the straight line passing through the averaged ΔT shifts (Fig. 2b). Curve processing for sample 2 (Fig. 1) yields $\beta \approx 1.4$, and the processing of analogous curves for sample 1 yields $\beta \approx 1.5$.

The resistances for both crystals decreased in a relatively narrow temperature range to a nonzero value; one can see in Fig. 1 that, starting at the level of ~0.1, a slanting tail appears. The same tail for sample 1 starts at a higher level of ~0.2. In this work, we will analyze only the upper portion of the transition, assuming that the electron spectrum is rearranged into the form typical of the superconducting state precisely in this region.

Figure 3 shows the $R(B)$ functions for very low temperatures $T/T_c < 0.05$. In this region, the normal resistance depends, though weakly, on the magnetic field, while the onset of transition is clearly defined and its shift is easily detected even upon changing the temperature below $T/T_c = 0.005$. When considering the $B_{c2}(T)$ functions in this region (see inset in Fig. 3), two facts are noteworthy. First, B_{c2} does not show a tendency to diverge near zero temperature; although the derivative of $B_{c2}(T)$ is large below 0.5 K, the function is linear within the experimental accuracy and is extrapolated to a finite value $B_{c2}(0)$ (a similar result was obtained previously for thallium crystals [6]). Second, the critical fields at low temperature are equal to 69 and 80 kOe for samples 1 and 2, respectively; i.e., they differ by more than 10%, in spite of the fact that the crystals were from the same batch and their T_c values coincided.

The graph of $B_{c2}(T)$ over the entire temperature range is shown in the inset in Fig. 4; as in other HTSC cuprates, the second derivative $\partial^2 B_{c2}/\partial T^2 \geq 0$ for all temperatures (cf., e.g., [6, 7]).

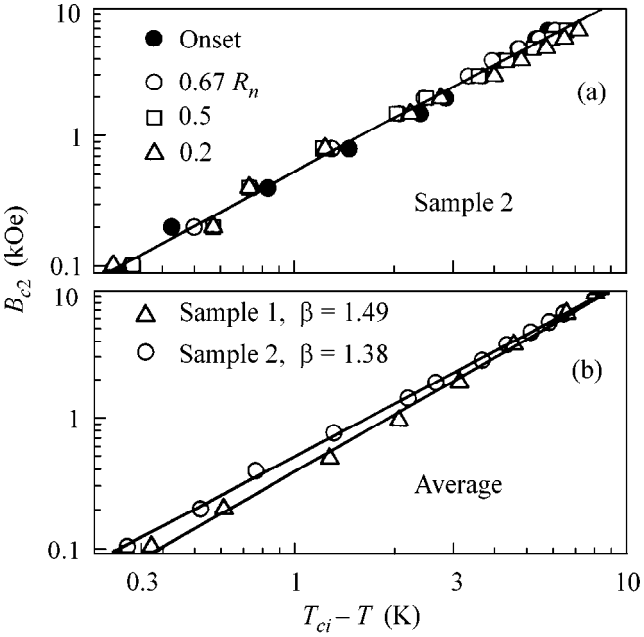

Fig. 2. (a) Plots of the field vs. shift at different levels in this field; (b) the same for the averaged shifts for two samples.

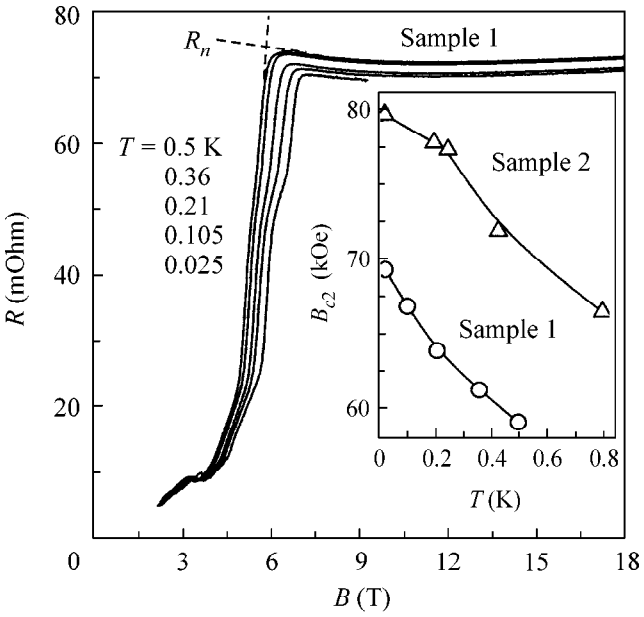

Fig. 3. The $R(B)$ curves for sample 1 at temperatures (from left to right) from 0.5 K to 25 mK. Inset: the field of the onset of transition at low temperatures for both samples.

Discussion. It follows from the preceding section that our data for the vicinity of T_c are consistent, within the experimental accuracy, with Eq. (2). It would have been instructive to compare these data with the data on heat capacity, but, unfortunately, in the works where the heat capacity of $Nd_{2-x}Ce_xCuO_{4-y}$ was measured [15], the contribution of critical fluctuations near T_c was not

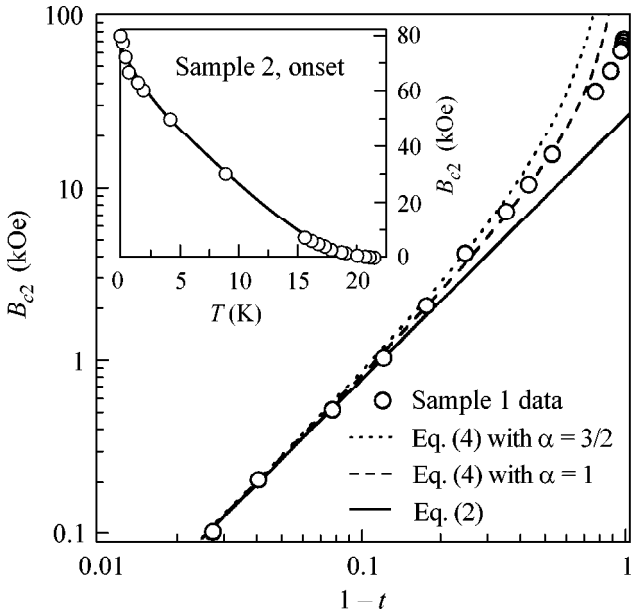

Fig. 4. Comparison of the experimental B_{c2} values for sample 1 with Eqs. (2) and (4). Inset: the $B_{c2}(T)$ function for sample 2 over the entire temperature range. The line is a guide to the eye.

determined. Nevertheless, it is known that the measurements of heat capacity of HTSC materials show strong dissimilarities to usual superconductors [16] but do not allow the discrimination between the BCS and BEC models. These problems can be illustrated by comparing the results of measurements of the resistance and heat capacity of the thallium high-T_c superconductor. No explicit jump in heat capacity is observed for this compound even at zero field, although the contribution from the critical fluctuations is undoubtedly present in the temperature range 16–10 K [17]; this contribution is reduced by approximately one-half in a field of 0.4 T and remains virtually unchanged with changing temperature. At the same time, the resistive measurements made by the same experimental group [6] suggest that a field of 0.4 T shifts the transition by 25% from 16 to 12 K.

In connection with this contradiction, an interesting remark was made in [18], where numerical calculations were carried out for the heat capacity of an ideal charged Bose gas in a weak magnetic field. It is well-known that BEC does not occur in an ideal charged Bose gas in a uniform magnetic field [19], because the density of states diverges at the lower Landau level of the spectra of charged bosons. This implies that the transition occurs only at an isolated point in the (T, B) plane. The magnetic field in this plane is scaled by the comparison of the cyclotron energy $\hbar eB/mc$ with T_c. Substituting the free electron charge and mass for e and m, respectively, one arrives at the value of 8 T for the characteristic field at T_c = 16 K. On this scale, the above-mentioned field of 0.4 T is as small as 0.05. As long as the field is low, the phase trajectory again passes through the vicinity of the transition point in the (T, B) plane upon changing T, but, as the field increases, the "impact parameter" increases, while the contribution of critical fluctuations decreases. However, the temperature interval corresponding to the small impact parameters does not change. In the case that the transition is BEC in a weakly nonideal charged Bose gas, this contribution is hidden from view at the lower temperature where the transition occurs in a magnetic field. Then, strange as it may seem, resistive measurements provide more reliable information on the transition position than heat capacity measurements do.

According to the results obtained for the immediate vicinity of T_c, the behavior of the $B_{c2}(T)$ function should be compared with the predictions of the superconductivity models in a nonideal Bose gas. Due to boson scattering by impurities or to the boson–boson interaction, the critical field in a weakly nonideal Bose gas behaves as [20]

$$B_{c2} \propto t^{-\alpha}(1 - t^{3/2})^{3/2}, \quad t = T/T_c, \tag{4}$$

where, depending on the particular model, the exponent α is equal to 1 or 3/2 [20, 21]. At $t \longrightarrow 1$, function (4) takes the asymptotic form (2). It is seen in Fig. 4 that the experimental points deviate in the proper direction from the asymptote and, on the whole, correspond well to Eq. (4). A more detailed comparison is hardly pertinent, as long as the theories [20, 21] do not allow for field-induced pair decay into fermions.

Conclusions. The field-induced distortion of the shape of the resistive superconducting transition in the $Nd_{2-x}Ce_xCuO_{4-y}$ single crystals is appreciably smaller than the transition shift. This allows the measurement of the $B_{c2}(T)$ function. As T_{c0} is approached, the B_{c2} field behaves as a power function $B_{c2} \propto (\Delta T)^{\beta}$ with $\beta \approx 1.5$ and, correspondingly, with a horizontal tangent $\partial B_{c2}/\partial T = 0$. This should imply the absence of a jump in heat capacity at the zero-field phase transition. Such behavior is precisely that which is expected for the heat capacity and critical field in BEC of a charged Bose gas. For this reason, one of the possible conclusions that can be drawn from such behavior of $B_{c2}(T)$ near T_c is that the description of superconductivity of HTSC materials should involve the BEC elements, i.e., should make allowance for the fact that fermions near the Fermi level tend to form bosons at temperatures above T_c. The T dependence of B_{c2} persists down to the lowest temperatures, although the B_{c2} values in this region probably depend on lattice defects.

We are grateful to A.A. Abrikosov, L.P. Gor'kov, and V.P. Mineev for helpful discussions. The experiments at the NHMFL were performed in the framework of the program of cooperation between the NHMFL and scientists from the former USSR. This work was supported by the Russian Foundation for Basic Research (project no. 99-02-16117), the Russian Foundation for Basic Research–PICS (project no. 98-02-22037), State

Contract 107-2(00)-P, and the program "Statistical Physics" of the Ministry of Sciences of the Russian Federation.

REFERENCES

1. J. R. Waldram, *Superconductivity of Metals and Cuprates* (Institute of Physics, 1996).
2. V. Emery and S. Kivelson, Nature (London) **374**, 434 (1995).
3. L. V. Ioffe and A. J. Millis, Phys. Rev. B **54**, 3645 (1996).
4. V. B. Geshkenbein, L. B. Ioffe, and A. I. Larkin, Phys. Rev. B **55**, 3173 (1997).
5. N. R. Werthamer, E. Helfand, and C. Hohenberg, Phys. Rev. **147**, 295 (1966).
6. A. P. Mackenzie, S. R. Julian, G. G. Lonzarich, *et al.*, Phys. Rev. Lett. **71**, 1238 (1993); A. Carrington, A. P. Mackenzie, D. C. Sinclair, and J. P. Cooper, Phys. Rev. B **49**, 13243 (1994).
7. M. S. Osofsky, R. J. Soulen, Jr., S. A. Wolf, *et al.*, Phys. Rev. Lett. **71**, 2315 (1993); J. Supercond. **7**, 279 (1994).
8. M. Suzuki and M. Hikita, Jpn. J. Appl. Phys. **28**, L1368 (1989).
9. Y. Hidaka and M. Suzuki, Nature (London) **338**, 635 (1989); M. Suzuki and M. Hikita, Phys. Rev. B **41**, 9566 (1990).
10. Y. Dalichaouch, B. W. Lee, C. L. Seaman, *et al.*, Phys. Rev. Lett. **64**, 599 (1990).
11. S. H. Han, C. C. Almasan, M. C. de Andrade, *et al.*, Phys. Rev. B **46**, 14290 (1992).
12. D. J. C. Walker, O. Laborde, A. P. Mackenzie, *et al.*, Phys. Rev. B **51**, 9375 (1995).
13. V. F. Gantmakher, G. É. Tsydynzhapov, L. P. Kozeeva, and A. N. Lavrov, Zh. Éksp. Teor. Fiz. **115**, 268 (1999) [JETP **88**, 148 (1999)].
14. L. D. Landau and E. M. Lifshitz, *Statistical Physics* (Nauka, Moscow, 1964; Pergamon, Oxford, 1980).
15. E. Maiser, W. Mexner, R. Schäfer, *et al.*, Phys. Rev. B **56**, 12961 (1997).
16. A. Junod, M. Roulin, B. Revaz, and A. Erb, Physica B (Amsterdam) **280**, 214 (2000).
17. A. Carrington, A. P. Mackenzie, and A. Tyler, Phys. Rev. B **54**, R3788 (1996).
18. A. S. Alexandrov, W. H. Beere, V. V. Kabanov, and W. Y. Liang, Phys. Rev. Lett. **79**, 1551 (1997).
19. M. R. Shafroth, Phys. Rev. **100**, 463 (1955).
20. R. Micnas, J. Ranninger, and S. Robaszkiewicz, Rev. Mod. Phys. **62**, 113 (1990).
21. A. S. Alexandrov, Phys. Rev. B **48**, 10571 (1993).

Translated by V. Sakun

JETP Letters, Vol. 72, No. 1, 2000, pp. 26–29. Translated from Pis'ma v Zhurnal Éksperimental'noĭ i Teoreticheskoĭ Fiziki, Vol. 72, No. 1, 2000, pp. 39–44.

Magnetic Properties of Two-Dimensional Josephson Networks: Self-Organized Criticality in Magnetic Flux Dynamics

S. M. Ishikaev*, É. V. Matizen*, V. V. Ryazanov, V. A. Oboznov**, and A. V. Veretennikov****

** Institute of Inorganic Chemistry, Siberian Division, Russian Academy of Sciences, pr. Akademika Lavrent'eva 3, Novosibirsk, 630090 Russia*

*** Institute of Solid-State Physics, Russian Academy of Sciences, Chernogolovka, Moscow region, 142432 Russia*
e-mail: ryazanov@issp.ac.ru

Received June 7, 2000

The field dependence of the magnetic moment of square (100 × 100) Josephson networks was examined with the use of a SQUID magnetometer. The field dependence of the magnetic moment was found to be regular with features corresponding to integer and half-integer numbers of flux quanta per cell. At temperatures below 5.8 K, jumps in the magnetization curves associated with the entry and exit of avalanches of tens and hundreds of fluxons were observed. It was shown that the probability distribution of these processes corresponded to the theory of self-organized criticality. An avalanche character of flux motion was observed at temperatures at which the size of the fluxons did not exceed the size of the cell, that is, when a discrete vortex structure occurred. © *2000 MAIK "Nauka/Interperiodica".*

PACS numbers: 85.25.Cp; 74.25.Ha; 74.50.+r; 74.60.Ge

Two-dimensional regular Josephson junction networks arouse intense interest because of specific features of vortex dynamics in these discrete superconducting systems [1, 2] and because of the possibilities of their practical use as sources of coherent millimetric radiation [3] and elements of logic units [4]. Even though a number of theoretical articles devoted to the magnetic properties of such networks have been published [5, 6], experimental studies of the magnetic properties of Josephson junction networks are actually lacking.

We studied square 100 × 100 Josephson junction networks with a cell of size $a^2 = 20 \times 20\ \mu m^2$ (a network fragment is schematically depicted in Fig. 1). Underdamped Nb–NbO_x–Pb Josephson tunnel junctions [7] had an area of 7 μm^2 and the following characteristics at $T = 4.2$ K: critical current $I_c \approx 150\ \mu A$ and normal resistance $R_n \approx 10\ \Omega$ (see inset in Fig. 1).

The measurement of magnetic dynamics even in such relatively large, two-dimensional arrays of Josephson junctions with 10^4 cells required that the SQUID magnetometer at our disposal had to be essentially updated. The pickup coils of the flux transformer were made in the form of a symmetric second-order gradiometer [8]. As distinct from the classical circuit, the central coil was divided into two identical separated coils [9]. This offered some preferences, providing, in particular, a significantly weaker dependence of the signal on the position of the sample. The astaticism of the pickup coils was about 3×10^{-4}. An additional coil of several copper wire turns was used for fine compensation. A current proportional to the solenoid current was passed through this coil during operation. The slope of the magnetization curves can be varied by varying the proportionality factor. This allowed the weak signal ~10^{-10} A m^2, which is directly related to the dynamics of the magnetic field in the network, to be distinguished. Thus, the intrinsic contribution of the superconducting Nb and Pb films in the structure under study was compensated to a maximum extent in the magnetization curves presented below. To diminish drifts and interferences, the liquid

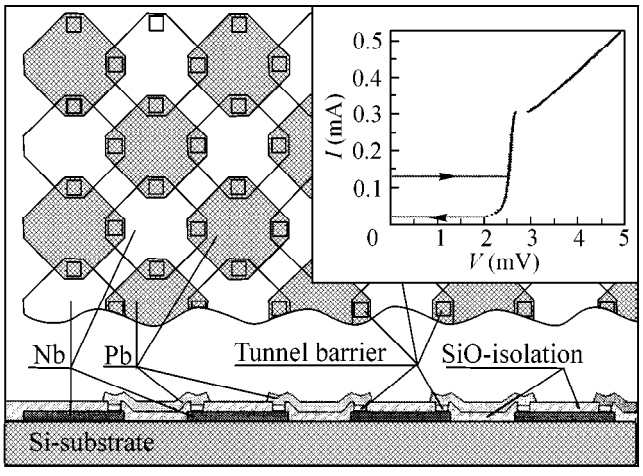

Fig. 1. Geometry of a Josephson Nb–NbO_x–Pb junction network. The inset shows the voltage–current characteristic of an individual junction at $T = 4.2$ K.

helium in the volume containing the flux transformer, the solenoid, and a superconducting magnetic screen was transferred to a superfluid state by pumping the vapor out.

A set of magnetization curves for the Josephson junction array measured at various temperatures is shown in Fig. 2. A regular structure is well pronounced in all the curves at temperatures below T_c of Pb (7.2 K) with a temperature-independent magnetic-field period equal to approximately 60 mOe. With allowance made for the screening of the solenoid field by the superconducting film structure, this value satisfactorily corresponds to the flux quantum per cell $\Delta H = \Phi_0/a^2 \approx$ 50 mOe, where Φ_0 is the magnetic flux quantum and a is the network period. Small features are also apparent that correspond to a magnetic flux equal to one-half the quantum per cell. Large hysteresis loops at temperatures of 6.0 and 6.8 K were obtained by double passage. To demonstrate the reproducibility, two loops with a smaller field swing are also presented. It is evident that all these curves are perfectly superimposed on each other.

The behavior of the magnetic moment of the Josephson junction network at temperatures below 5 K is of special interest. Pronounced jumps in the magnetic moment appear in the hysteresis loops. These jumps increase with decreasing temperature. The jumps with the maximum amplitude form periodic compact groups arranged in the vicinity of the magnetic flux values corresponding to an integer number of quanta per cell ("integer frustrations" $f = \Phi/\Phi_0 = 0, 1, 2, \ldots$). Magnetization curves recorded in detail at $T = 2.1$ K in the region $f = 0$ upon varying the external field within the range ±25 mOe, which encloses one group of flux jumps, are shown in Fig. 3. It is evident that jumps occur at random field values, and their amplitudes have a significant scatter. Such behavior, even though it resembles thermal noise, is not of this kind, if only because the processes of origination and relaxation of unstable states are enhanced with decreasing temperature. Each of the jumps in the magnetic moment noticeable in the figure corresponds to the simultaneous entry (or exit) of avalanches of tens and hundreds of flux quanta in the network. To illustrate this fact, in addition to the main scale, a magnetic flux quantum scale is presented in the plot. Distinctive features of the flux jumps are a very short time of the transient process (much less than the characteristic response time of our recording system, 0.1 s) and their definite direction. The character of the jumps observed does not depend on the magnetic field sweep rate within three orders of magnitude 0.01–10 mOe/s. (At a rate of 10 mOe/s, the recording system already had no time to follow the jumps and all acute angles in the curves adjacent to the vertical drops became smoothed and fuzzy.)

The dependence of the critical current on the magnetic field was directly measured in transport studies of 10 × 10 networks with close parameters [10]. The

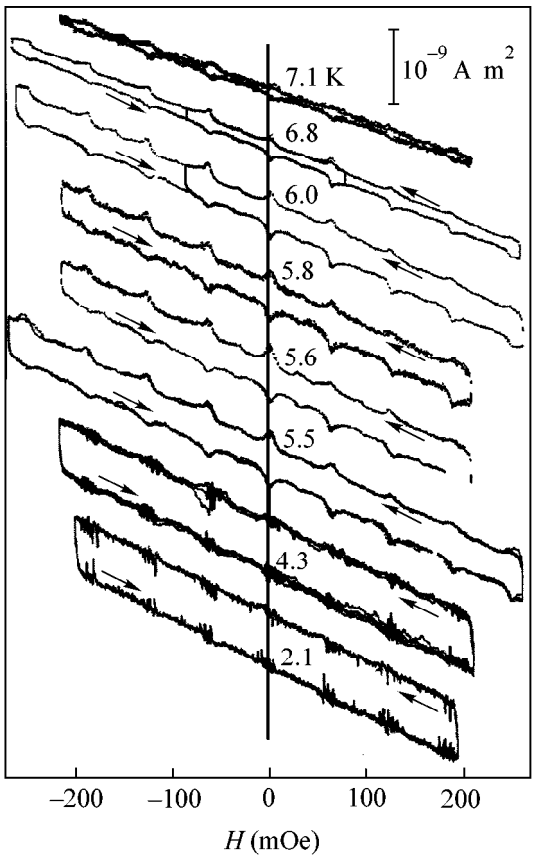

Fig. 2. Set of magnetization curves for a Josephson network measured at various temperatures.

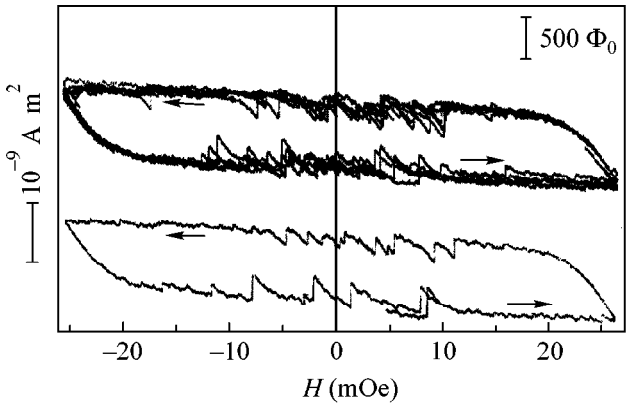

Fig. 3. Hysteresis loop in the region of small magnetic fluxes (0–$\Phi_0/2$ per cell) that encloses one group of avalanche breakdowns of the flux in the network.

curves obtained for temperatures above 5 K are qualitatively identical with the curves $M(H)$ presented in Fig. 2. The latter curves are also in good agreement with the calculations [5]. These curves are manifestations of the specific critical state occurring in this system. The periodic magnetic moment peaks correspond to the sharp increase in the critical current of fluxon

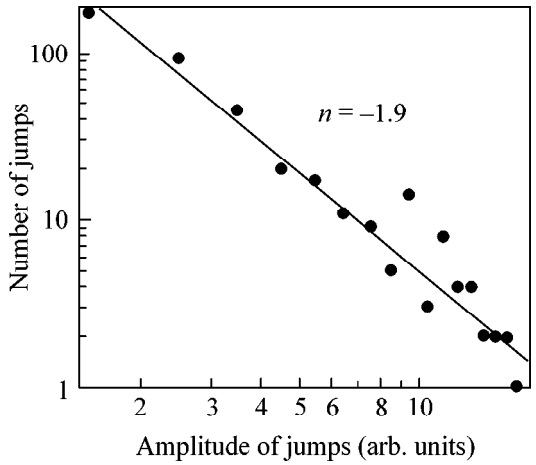

Fig. 4. Histogram of the dependence of the number of jumps on their amplitudes confirming the power law of the probability distribution of processes.

pinning (depinning current) at integer-valued frustrations, when the flux state in the network is most stable. In resistive studies [10], as well as in magnetization curves, small features are also manifested at half-integer values of f, when the flux fills the network cells in a staggered order [11]. The fluxon depinning current at half-integer frustrations can be evaluated from the half-widths of hysteresis loops with the use of the simplified assumption that currents in the network flow along concentric square circuits: $I_p(6.8\ \mathrm{K}) = 0.9\ \mu\mathrm{A}$, $I_p(6.0\ \mathrm{K}) = 2.5\ \mu\mathrm{A}$, $I_p(5.8\ \mathrm{K}) = 2.9\ \mu\mathrm{A}$, $I_p(5.5\ \mathrm{K}) = 3.3\ \mu\mathrm{A}$, $I_p(4.3\ \mathrm{K}) = 4.6\ \mu\mathrm{A}$, and $I_p(2.1\ \mathrm{K}) = 4.7\ \mu\mathrm{A}$. It is evident that the real current lines cut off the corners of the squares; therefore, the value obtained from the simplest model is somewhat overestimated. The excess depinning current at the peaks arising at integer f over the values for intermediate f ("at the pedestal") decreases with decreasing temperature. This is associated with the enhancement of the self-field effects of currents [12, 13] that arise as the fluxon radius $\lambda = \Phi_0/2\pi\mu_0 I_c$ approaches the network parameter a. At temperatures when λ exceeds a, each fluxon extends over several cells and the self-fields of fluxons are small. For the structure under study, $\lambda(T)$ becomes markedly smaller than $a = 20\ \mu\mathrm{m}$ at $\lambda/a = 5.5$ K. At this temperature, the depinning current at the peaks is nearly twice as large as its value at the pedestal and is about $0.3I_c$ (I_c is the critical current of an individual junction). This is in agreement with the results [12] for $\lambda/a = 0.5$. At low temperatures (below 4.3 K), the height of the peaks in reference to the pedestal becomes insignificant, which corresponds to the transition to a discrete system of fluxons.

The fluxon avalanche breakdowns described above are a specific feature of the low-temperature dynamics of discrete fluxons. Below, we will show that these breakdowns resemble sand pile growth dynamics [14], which was the first model subject of the self-organized criticality theory [15]. This universal theory describes the behavior of a wide range of complex interactive systems attaining a critical state in their evolutionary process. This critical state becomes subsequently self-sustaining; that is, it requires no precision adjustment of external parameters for its existence. Up to now, experimental data on self-organized criticality have been obtained for a limited set of physical objects [14, 16, 17] in spite of the great interest in this problem and a great number of theoretical works (for example, [18–20]), some of which are devoted to self-organized criticality in superconducting systems [21–25]. A conventional critical state in hard superconductors, in principle, can possess the properties of self-organized criticality as was shown in model [21], which takes into account the discreteness of the effects of pinning centers on the Abrikosov vortices. However, the Josephson network is undoubtedly the best candidate for a discrete version of a type II superconductor. It was shown in [22–25] that, in the case when $V = a/\lambda \gg 1$, the continuum approximation is inapplicable and the Josephson medium transforms to a system in which pinning is accomplished in elementary circuits within one network cell. Taking into account that the inductance L of a Josephson network cell equals $\mu_0 a$ by the order of magnitude, one may rewrite the condition $V \gg 1$ as $2\pi L I_c \gg \Phi_0$, which corresponds to the ability of the cell to retain several magnetic flux quanta. In this case, provided that the size of the Josephson junction network is sufficiently large, the ensemble of fluxons in the network is a complex system of interacting elements possessing a great number of metastable states, which is equivalent to the classical Abelian sand pile model [20]. In a slowly varying magnetic field, the fluxon system attains an unstable state as the currents approach their critical value, from which it passes to one of the numerous metastable states under the action of random perturbations. The final state in which the system ends up after each of these jumps is determined by the number of metastable states in the system, their configuration, and the dynamics of collective fluxon motion in the network. Here, we note once again the fact that the jumps have the largest amplitudes predominantly in the vicinity of the field values at which the depinning current is a maximum. This allows the system to attain strongly nonequilibrium states, from which it recovers with the formation of large avalanches (Fig. 3). A histogram of the dependence of the number of jumps on their amplitudes constructed for $T = 2.1$ K demonstrates a power law that serves as the "trademark" of self-organized criticality. The power $n = -1.9 \pm 0.1$. Close values, i.e., –1.75 and 1.80, were obtained in [22] by a computer simulation of a one-dimensional Josephson network (one-dimensional multiple-contact SQUID) for structures containing 256 and 128 cells, respectively.

Note in conclusion that Josephson junction networks are in principle perfect model subjects for studying self-organized criticality. The networks can be prepared with precisely specified parameters like period,

number of cells, and critical current of junctions, whereas the magnitude of the critical current can be varied within some limits directly during the experiment by varying the temperature. In addition to studying the magnetic and resistive properties of Josephson networks, electromagnetic radiation due to magnetic flux motion can also be measured. Comprehensive quantitative measurements and a detailed statistical analysis are necessary for a reliable corroboration and further investigations of processes of self-organized criticality in these structures. This analysis should include, for example, studying the scaling properties of the fluxon system in Josephson networks upon varying their sizes.

The authors are grateful to P.P. Bezverkhiĭ and V.G. Martynets for help in manufacturing photomasks of the networks and also to M.A. Lebedkin for useful discussions and comments.

This work was supported by the State Program High-Temperature Superconductivity and by INTAS, project no. 97-1940.

REFERENCES

1. C. J. Lobb, Physica B+C (Amsterdam) **126**, 319 (1984); D. W. Abraham, C. J. Lobb, and M. Tinkham, Phys. Rev. B **27**, 150 (1983).
2. H. S. J. van der Zant, F. C. Fritschy, T. P. Orlando, and J. E. Mooij, Europhys. Lett. **18**, 343 (1992); Phys. Rev. B **47**, 295 (1993); H. S. J. van der Zant, F. C. Fritschy, W. J. Elion, *et al.*, Phys. Rev. Lett. **69**, 2971 (1992); C. D. Chen, P. Delsing, D. B. Haviland, *et al.*, Phys. Rev. B **51**, 15645 (1995).
3. P. Barbara, A. B. Cawthorne, S. V. Shitov, and C. J. Lobb, Phys. Rev. Lett. **82**, 1963 (1999).
4. K. K. Likharev and V. K. Semenov, IEEE Trans. Appl. Supercond. **1**, 13 (1991).
5. D. Domínguez and J. V. José, Phys. Rev. B **53**, 11 692 (1996).
6. D.-X. Chen, J. J. Moreno, and A. Hernando, Phys. Rev. B **53**, 6579 (1996); D.-X. Chen, A. Sanchez, and A. Hernando, Phys. Rev. B **50**, 10 342 (1994).
7. V. A. Oboznov and A. V. Ustinov, Phys. Lett. A **139**, 481 (1989).
8. G. L. Romani, S. J. Williamson, and L. Kaufman, Rev. Sci. Instrum. **53**, 1815 (1982).
9. S. M. Ishikaev (in press); S. M. Ishikaev and E. V. Matizen, in *High Temperature Superconductivity: New Materials and Properties, Joint Symposium of the SB RAS and the CNEAS TU, Tohoku University, Japan, 1999*, p. 65.
10. G. Yu. Logvenov, V. A. Oboznov, V. V. Ryazanov, and A. V. Ustinov, Czech. J. Phys. **46**, 687 (1996).
11. L. N. Vu, M. S. Wistrom, and D. J. van Harlingen, Appl. Phys. Lett. **63**, 1693 (1993); M. S. Rzchowski, S. P. Benz, M. Tinkham, and C. J. Lobb, Phys. Rev. B **42**, 2041 (1990).
12. T. E. Trias, J. R. Philips, H. S. J. van der Zant, and T. P. Orlando, IEEE Trans. Appl. Supercond. **5**, 2707 (1995).
13. J. R. Philips, H. S. J. van der Zant, J. White, and T. P. Orlando, Phys. Rev. B **47**, 5219 (1993).
14. G. A. Held, D. H. Solina, D. T. Keane, *et al.*, Phys. Rev. Lett. **65**, 1120 (1990).
15. P. Bak, C. Tang, and K. Wiesenfeld, Phys. Rev. Lett. **59**, 381 (1987); Phys. Rev. A **38**, 364 (1988).
16. H. J. S. Feder and J. Feder, Phys. Rev. Lett. **66**, 2669 (1991).
17. M. A. Lebyodkin, Y. Brechet, Y. Estrin, and L. P. Kubin, Phys. Rev. Lett. **74**, 4758 (1995); M. A. Lebedkin and L. R. Dunin-Barkovskiĭ, Zh. Éksp. Teor. Fiz. **113**, 1816 (1998) [JETP **86**, 993 (1998)].
18. H. Takayasu and Matsuzaki, Phys. Lett. A **131**, 244 (1988); J. M. Carlson and J. S. Langer, Phys. Rev. Lett. **62**, 2632 (1989); Phys. Rev. A **40**, 6470 (1989); K. Chen, P. Bak, and S. P. Obukhov, Phys. Rev. A **43**, 625 (1991).
19. J. Kertesz and L. B. Kiss, J. Phys. A **23**, L433 (1990).
20. D. Dhar, Phys. Rev. Lett. **64**, 1613 (1990).
21. O. Pla and F. Nori, Phys. Rev. Lett. **67**, 919 (1991).
22. S. L. Ginzburg, Zh. Éksp. Teor. Fiz. **106**, 607 (1994) [JETP **79**, 334 (1994)].
23. S. L. Ginzburg and N. E. Savitskaya, Pis'ma Zh. Éksp. Teor. Fiz. **68**, 688 (1998) [JETP Lett. **68**, 719 (1998)].
24. S. L. Ginzburg, M. A. Pustovoit, and N. E. Savitskaya, Phys. Rev. E **57**, 1319 (1998).
25. S. L. Ginzburg and N. E. Savitskaya, Zh. Éksp. Teor. Fiz. **117**, 227 (2000) [JETP **90**, 202 (2000)].

Translated by A. Bagatur'yants

JETP Letters, Vol. 72, No. 1, 2000, pp. 4–6. Translated from Pis'ma v Zhurnal Éksperimental'noĭ i Teoreticheskoĭ Fiziki, Vol. 72, No. 1, 2000, pp. 8–12.

Oscillations of the Crystallization Front of Adsorbed Water

V. G. Myagkov

Kirenskii Institute of Physics, Siberian Division, Russian Academy of Sciences, Akademgorodok, Krasnoyarsk, 660036 Russia

Received May 26, 2000

Relaxation oscillations of the crystallization front in a gradient temperature field have been observed for water adsorbed on a metal film deposited on a glass substrate. The metal film plays an important role in heat removal from the crystallization front and determines the existence of oscillations. A possible mechanism is proposed for the development of oscillations. It is shown that the oscillations observed are similar to the oscillations of the front of self-propagating high-temperature synthesis. © *2000 MAIK "Nauka/Interperiodica".*

PACS numbers: 64.70.Dv; 61.90.+d

In recent years, stable interest has been expressed to studying the development of morphological instabilities and dendritic growth in crystallization [1–3]. An analysis of linear stability made in [4] has become classical. However, it does not consider the periodic variation of the crystallization front velocity v_f, which can explain the appearance of the banded structure. This structure is often observed in metal alloys at high cooling rates [5, 6]. It consists of two successively alternating subbands that differ in microstructure and are aligned parallel to the crystallization front (CF). A typical period of the banded structure is of the order of 1 μm. The theory of CF stability was extended in [7] under the assumption that the distribution coefficient k_E depends on the velocity v_f. When the function $k_E(v_f)$ strongly depends on the value of v_f, the theory predicts the appearance of oscillatory instabilities of the CF for large values of v_f. Further development of the theory explaining the existence of oscillatory instabilities of the CF was obtained in [8, 9]. In [9], the diffusion of the latent heat liberated at the CF was taken into account. The main result of [9] was the conclusion that the development of the banded structure has its origin in CF oscillations, which arise when the velocity v_f decreases below the critical velocity v_c. For the values of the velocity v_f close to v_c, the oscillation amplitude λ grows as $\lambda \sim \sqrt{v_c - v_f}$; then, with decreasing v_f, the CF oscillations develop into relaxation oscillations. A further decrease in the velocity v_f leads to the Feigenbaum cascade of successive period-doubling bifurcations and further to chaotic oscillations. In this case, the oscillation wavelength is comparable to the temperature wavelength

$$\lambda \sim \sqrt{K_T \tau_{osc}}, \tag{1}$$

where τ_{osc} is the oscillation period, and K_T is the thermal diffusivity.

In [10], oscillatory instabilities were predicted within the phase-field model for the rapid directional solidification of a binary alloy.

Only a few of the general class of phenomena with moving boundaries known as the Stefan problem are characterized by oscillatory front instabilities. Among these are the existence of self-oscillating modes of an explosive crystallization front [11] and the existence of the front of self-propagating high-temperature synthesis (SHS) [12]. A linear analysis of the thermal stability of stationary modes made in [13, 14] determined the existence domains of self-oscillating modes of the explosive crystallization front. In [14], the oscillation wavelength λ of the explosive crystallization front was determined as

$$\lambda = 6.1 K_T / v_f. \tag{2}$$

Previously, similar problems were solved for the SHS front. In [15], the oscillation wavelength was estimated as

$$\lambda \cong 10 K_T / v_f. \tag{3}$$

A similar value of λ was obtained in [16]:

$$\lambda = 2\pi K_T / v_f. \tag{4}$$

For the SHS front and the explosive crystallization front, the numerical solutions found in [14–16] showed that, as the sample temperature T_S decreases and approaches the initiation temperature T_0, oscillations also exhibit a sequence of period doubling. Because the average velocity v_f of the CF may be defined as $v_f = \lambda/\tau_{osc}$, Eqs. (1)–(4) coincide to a constant factor and reflect the thermal mechanism of the propagation of oscillatory instabilities common to all the phenomena considered above.

It is known that water at normal pressure crystallizes into the hexagonal phase (1*h*). Depending on pressure and temperature, 12 polymorphous modifications, and at least 2 amorphous modifications, of ice exist (see,

e.g., [16, 17]). Investigations into the phase composition of water condensed onto cooled substrates indicate that the amorphous phase is formed at normal pressure at temperatures below 113 K [18].

This work is devoted to obtaining experimental evidence for the existence of oscillations of the adsorbed water CF. Samples were metal (nickel and tin) films about 30–50 nm thick deposited onto glass substrates 0.18 mm thick with linear sizes of ~5 × 15 mm. The samples were placed in a gradient temperature field at normal pressure and moisture. With decreasing sample temperature, a layer of water adsorbed from room air appeared on the substrate. On the side of the sample that had a low temperature, a CF that moved in the self-oscillating mode was formed (Fig. 1). Initially, when the cooling rate and the CF velocity were sufficiently large, the oscillation period and length were insignificant and the motion was of a chaotic character. As the CF approached a position with a temperature $T = 273$ K, its motion gained a pulsating mode and propagation was of a clearly defined relaxation character. In this case, the oscillation period was divided into rapid and slow parts. In the first part, the front jumped from one position to another at a velocity of ~ 0.1 m/s; next, in the second part, it stopped because of further cooling of the sample before the front. After that, the next jump occurred, and so forth (Fig. 1). The jump time τ_j was significantly shorter than the stop time τ_0 ($\tau_j \ll \tau_0$). Therefore, the oscillation period $\tau_{osc} = \tau_0 + \tau_j$ was determined by the stop time τ_0. As the CF approached a position with a temperature equal to the melting point $T_M = 273$ K, not only did the wavelength increase (Fig. 1), but the oscillation period increased as well. This behavior was likely determined by period doubling. These oscillations were observed visually or under low magnification.

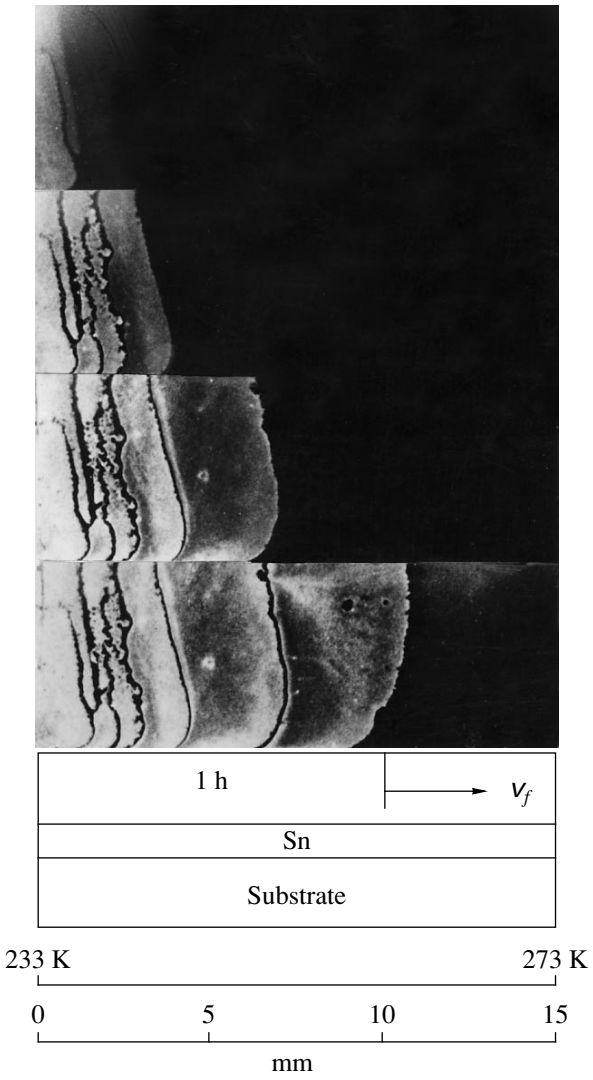

Fig. 1. Successive stages of the development of oscillations of the adsorbed water CF on the surface of a tin film (~40 nm in thickness) deposited on a glass substrate.

Two scenarios are possible for the development of oscillatory instabilities of the CF on solidification of water adsorbed on a glass surface covered with a metal film. In the first one, oscillations appear in the motion of the CF from the liquid phase and the oscillation length is determined by Eq. (1). The front velocity during the jump is comparable to the front velocity observed in explosive crystallization [11]. Therefore, one may suggest the second mechanism of the development of oscillatory instabilities in the crystallization of an adsorbed water layer. The crystallization temperature is slightly lower than the melting point $T_M = 273$ K. At substrate temperatures T_S, explosive crystallization with a wavelength of λ is initiated that obeys Eq. (2). It is known that the explosive crystallization of ice has the initiation temperature $T_0 \sim 113$ K and a very low velocity of front motion $v_f \sim (0.2–1) \times 10^{-2}$ m/s. However, molecular dynamics studies of supercooled water [19] showed that a multitude of amorphous states can be formed. In [20], a transition to the solid state through an amorphous phase was substantiated. Theories explaining the appearance of a layered structure were developed for binary alloys. These theories do not explain the existence of oscillations for pure substances. Therefore, the second scenario of the formation of oscillatory instabilities is more probable. This conclusion is confirmed by the existence of oscillations for directional crystallization in a given gradient temperature field. Similar oscillations are observed for explosive crystallization in the course of scanning over an amorphous semiconductor film with a laser beam [21].

The thermal mechanism for the appearance of oscillations is confirmed by experimental values of λ and τ_{osc}, which satisfactorily correspond to Eq. (1) with the coefficient $K_T = 5.0 \times 10^6$ m^2/s (Fig. 2). The value of K_T obtained exceeds the thermal diffusivity of water (0.13×10^6 m^2/s) by a factor of 40 and is smaller than the thermal diffusivity of the tin film (38×10^6 m^2/s) by

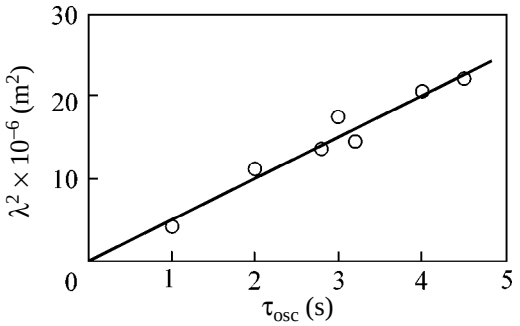

Fig. 2. Dependence of the wavelength λ on the oscillation period τ_{osc} of the adsorbed water CF on the sample surface depicted in Fig. 1.

almost an order of magnitude. This suggests that the metal film plays an important role in heat removal from the CF and determines the appearance threshold and the character of oscillations. Actually, oscillations of the adsorbed water CF were not observed in the absence of a metal film. Oscillations arise only on a freshly sputtered metal layer. The occurrence of oxides leads to degradation of the metal surface and to the termination of oscillations. If temperature noise with the average value $\langle \Delta T \rangle = 10$ K is superimposed on the constant temperature field under experimental conditions, then the CF exhibits spikes in the vicinity of an equilibrium position.

The propagation character of the oscillations of the adsorbed water CF described above is rather similar to the oscillations of the SHS front in thin films [22]. Multiple SHS (MSHS) [23] is a variety of SHS in thin films, which is different from SHS in powders. In [23], it is shown that MSHS is a reversible structural phase transition that corresponds to the eutectic crystallization of bulk samples. As distinct from eutectic solidification, MSHS in thin films occurs in the solid phase, and phase separation likely proceeds from the amorphous phase below the initiation temperature T_0. In this case, the eutectic temperature T_E of bulk samples is higher than the initiation temperature T_0 of MSHS. When temperature noise is superimposed, the MSHS front, as well as the adsorbed water CF, exhibits chaotic spikes in the vicinity of T_0. In [24], it is shown that low-energy excitations ($\epsilon \sim 100$ J/mol) are the basis of the structural instability that determines the mechanisms of chaotic spikes of the MSHS front and oscillations of the SHS front. This suggests a common mechanism of oscillatory instabilities for the CF of water adsorbed on a metal layer and for the SHS front in thin films. It follows from the above that the crystallization process in thin films significantly differs from the crystallization of bulk samples because of intense heat extraction into the substrate and may exhibit instabilities in CF propagation.

This work was supported by the Russian Foundation for Basic Research, project no. 99-03-32184.

REFERENCES

1. J. S. Langer, Rev. Mod. Phys. **52**, 1 (1980).
2. H. E. Stanly, in *Fractals and Disordered Systems*, Ed. by A. Bunde and S. Halvin (Springer-Verlag, Berlin, 1991).
3. M. C. Cross and P. C. Hohenberg, Rev. Mod. Phys. **65**, 851 (1993).
4. W. W. Mulins and R. F. Sekerka, J. Appl. Phys. **35**, 444 (1964).
5. W. J. Boettinger, D. Shechtman, R. J. Schalfer, and F. S. Biancaniello, Metall. Trans. A **15**, 55 (1984).
6. W. Kurz and R. Triverdi, Acta Metall. **38**, 1 (1990).
7. S. R. Coriell and R. F. Sekerka, J. Cryst. Growth **61**, 499 (1983).
8. M. Carrad, M. Gremad, M. Zimmermann, and W. Kurz, Acta Metall. **40**, 983 (1992).
9. A. Karma and A. Sarkissian, Phys. Rev. E **47**, 513 (1993).
10. M. Conti, Phys. Rev. E **56**, R6267 (1997).
11. V. A. Shklovskiĭ and V. M. Kuz'menko, Usp. Fiz. Nauk **157**, 311 (1989) [Sov. Phys. Usp. **32**, 163 (1989)].
12. A. G. Merzhanov and É. N. Rumanov, Usp. Fiz. Nauk **151**, 553 (1987) [Sov. Phys. Usp. **30**, 293 (1987)].
13. V. A. Shklovskiĭ, Zh. Éksp. Teor. Fiz. **82**, 536 (1982) [Sov. Phys. JETP **55**, 311 (1982)].
14. W. van Saarlos and J. D. Weeks, Physica D (Amsterdam) **12**, 279 (1984).
15. K. G. Shkadinskiĭ, B. I. Khaĭkin, and A. G. Merzhanov, Fiz. Goreniya Vzryva **7**, 19 (1971).
16. A. P. Aldushin, T. M. Martem'yanova, and A. G. Merzhanov, Fiz. Goreniya Vzryva **9**, 613 (1973).
17. H. Tanaka, Nature (London) **380**, 328 (1996).
18. L. G. Dovell and A. P. Rinfret, Nature (London) **360**, 120 (1960).
19. P. H. Poole, F. Sciortino, U. Essmann, and H. E. Stanley, Nature (London) **380**, 328 (1996).
20. P. J. Ortoleva, J. Phys. Chem. B **101**, 8324 (1997).
21. *Laser and Electron – Beam Processing of Materials*, Ed. by C. W. White and P. S. Peercy (Academic, New York, 1980).
22. V. G. Myagkov, L. E. Bykova, and V. A. Seredkin, Dokl. Akad. Nauk **363**, 762 (1998) [Dokl. Phys. **43**, 768 (1998)].
23. V. G. Myagkov, Dokl. Akad. Nauk **364**, 330 (1999) [Dokl. Phys. **44**, 45 (1999)]; V. G. Myagkov, L. E. Bykova, and G. N. Bondarenko, Zh. Éksp. Teor. Fiz. **115**, 1754 (1999) [JETP **88**, 963 (1999)].
24. V. G. Myagkov and L. E. Bykova, Dokl. Akad. Nauk (in press) [Phys. Dokl. (in press)].

Translated by A. Bagatur'yants

JETP Letters, Vol. 72, No. 1, 2000, pp. 7–10. Translated from Pis'ma v Zhurnal Éksperimental'noĭ i Teoreticheskoĭ Fiziki, Vol. 72, No. 1, 2000, pp. 13–17.

Study of the Ion Composition of an Expanding Magnesium Plasma Produced by a CO_2 Laser

K. N. Makarov*, S. G. Nishchuk*, V. K. Rerikh*, Yu. A. Satov*, I. Yu. Skobelev, Yu. B. Smakovskiĭ*, A. N. Starostin*, A. E. Stepanov*, T. A. Pikuz**, A. Ya. Faenov**, and S. V. Khomenko***

**Troitsk Institute of Innovation and Fusion Research, Troitsk, Moscow region, 142092 Russia*
e-mail: andreist@mtu-net.ru

***All-Russia Research Institute of Physicotechnical and Radio Metrology, Mendeleevo, Moscow region, 141570 Russia*

Received May 19, 2000

The evolution of the ion composition of a laser plasma during its expansion over a large distance is studied. The plasma is produced by a TIR CO_2 laser with a pulse energy up to 100 J and duration of ~20 ns. X-ray diagnostics with the use of a spectrograph and X-ray PIN diodes was applied to study the plasma near the target surface. At large distances from the target surface, time-of-flight neutral-particle diagnostics with the use of an electrostatic analyzer and ion collector was applied. Calculations performed with the GIDRA-1 code agree well with experimental data. © *2000 MAIK "Nauka/Interperiodica".*

PACS numbers: 52.70.La; 52.50.Jm

The generation of high-current beams of multicharged ions in a laser plasma attracts considerable interest in connection with the wide applications of such beams in accelerators of heavy particles, heavy-ion nuclear fusion research, material testing, and medicine. This problem requires an understanding of all the effects accompanying plasma evolution, starting from plasma heating by laser radiation to plasma expansion over the large distances that are needed to extract the ions. In particular, it is not quite clear to what extent the plasma recombines during expansion. In connection with this, it is necessary to measure the main plasma parameters, in particular, the ion composition both near the target and at a large distance from it. Since the plasma density near the critical surface and that at a distance of about one meter differ greatly, such measurements cannot be carried out using unified diagnostics. In this study, the ion composition of a laser plasma was determined by using the combination of space-resolved X-ray spectral measurements and the time-of-flight technique (Fig. 1).

Results presented in this paper were obtained with the TIR device at the Troitsk Institute of Innovation and Fusion Research [1]. The TIR is a CO_2 laser with an output energy up to 100 J. At present, the device operates by the "driving oscillator + amplifier" scheme, which allows us to obtain smooth pulses with a duration of 13–80 ns. The pulse duration is varied by changing the mode of the oscillator operation and the composition of cells with a saturating absorber (SF_6–air mixture). The radiation is focused on a target by a lens with F = 60 cm. The size of the focal spot is nearly 65 μm in the waist. Experiments described in this paper were carried out with a FWHM pulse duration of 20 ns.

Soft X radiation was recorded with the help of spectrographs with spherically curved mica crystals. The mica crystals, plasma, and a film were arranged according to the FSSR-1D scheme [2]. Spectra were obtained with high spectral ($\lambda/\Delta\lambda \simeq 10000$) and spatial ($\Delta x \simeq 20$ μm) resolution in the direction of plasma expansion. Figure 2 shows a spectral region near the resonant lines of He-like magnesium ions and densitograms obtained at different distances from the target surface.

The measurements of the X-ray spectrum were carried out with the target displaced 3 mm from the focal plane. When the target was located at the focus, we could not obtain high-quality spectrograms because of the intense exposure of the X-ray film by suprathermal

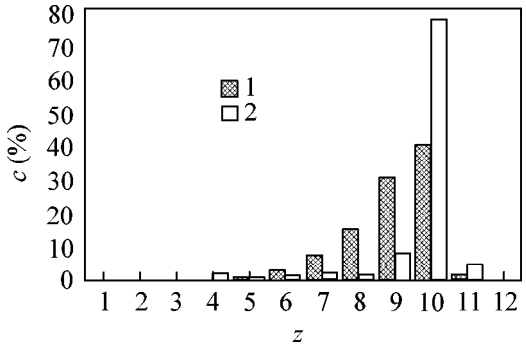

Fig. 1. (1) Experimental and (2) calculated distribution of ions over the degree of ionization at a distance of 3 m from the target surface.

0021-3640/00/7201-0007$20.00

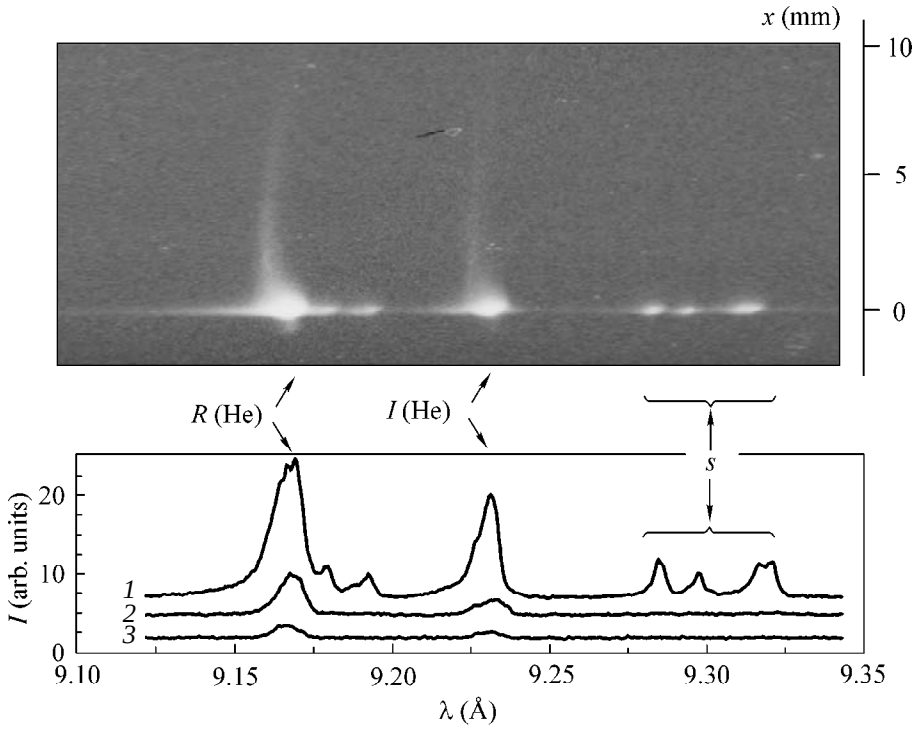

Fig. 2. Spectral region near the resonant lines of He-like Mg ions (top) and its densitograms at different distances from the target (bottom): (*1*) 0, (*2*) 0.5, and (*3*) 1 mm.

electrons. For a target displaced from the focal plane, the laser spot diameter can be estimated as D_f = 200–300 μm and the corresponding radiation-power density as $P_0 = 10^{12}$–10^{13} W/cm^2.

Calculations were performed by the GIDRA-1 one-dimensional code. A detailed analysis of spectral measurements for a magnesium target irradiated by pulses of XeCl and Ne lasers and descriptions of the physical and numerical models were presented in [3, 4]. In this study, all the calculations were conducted assuming spherical geometry; as was shown previously, this assures a qualitative agreement between the calculated and experimental data. The total number of states in the model of the magnesium atom was 77. Self-absorption of spectral lines was taken into account in terms of the probability of photon emission. The emission probability was calculated by Sobolev's model [5].

The optical scheme and the procedure of spectrum processing were such that the obtained dependences of the spectral-line intensities on the distance along the normal to the target surface were integral over both time and the cross section of the expanding plasma. Therefore, the recorded intensity at a distance x from the target within a small interval dx was proportional to the time-integrated power radiated by a plasma layer with the same thickness:

$$P_{\text{exp}}(x) = \int_0^\infty dt \int_{-\infty}^{+\infty} L_{\text{exp}}(x, y, t)dy. \qquad (1)$$

Assuming the plasma expands in a certain cone, we should take into account that the recorded line intensity is proportional to the volume emission intensity multiplied by x^2. With regard to this fact, in treating the results of one-dimensional calculations performed in spherical geometry, we used the formula

$$\bar{P}_{\text{sim}}(r) = \int_0^\infty r^2 L_{\text{sim}}(r, t)dt, \qquad (2)$$

which qualitatively accounts for the geometric factor mentioned above. The intensity was additionally averaged over a distance of 40 μm, taking into account the spatial resolution of the spectrograph, film, and scanner.

Figure 3a shows the measured intensities of the resonant and intercombination lines as a function of the distance from the target surface; the intensities were obtained by scanning the spectrum. The characteristic feature of the X-ray spectrum under our experimental conditions is the nearly identical intensity of the resonant and intercombination lines at a large distance from the target. Such behavior of the intensities of these two lines is not typical. Under conditions of irradiation by either a neodymium laser (SATELLITE, All-Russia Research Institute of Physicotechnical and Radio Metrology [6]) or an excimer laser (HERCULES, λ = 0.308 μm, ENEA, Frascati, Italy [7]), the characteristic feature is that the intensity of the intercombination line is dominant at relatively large distances from the target and

even a second maximum arises in the radiation intensity at a distance of 1–2 mm from the target. The physical reasons why this maximum arises were analyzed in [3]. These are the formation of a compression wave during plasma expansion and, probably, an insufficiently high vacuum in the interaction chamber; the latter could enhance the effect of the compression wave. Under our experimental conditions, the line intensities fall monotonically as the distance from the target increases.

Figure 3b shows the calculated integral distributions of the intensities of the resonance lines of He-like magnesium ions along the normal to the target surface. The somewhat smaller width of the calculated peaks is explained by the fact that, on the one hand, we used the one-dimensional gas-dynamic model and, on the other hand, the experimental spectrum was measured from shot to shot, in several pulses. We note that, in the calculations, the ratio of the peak intensities of the resonant lines increases as the power density of the laser pulse increases; therefore, it can be suggested that there are high-temperature areas on the target surface.

Figure 4 shows the spatial distributions of the plasma parameters at the instant of the maximum laser power; the peak power density of laser radiation on the surface of a solid target is $P_0 = 6.25 \times 10^{12}$ W/cm^2; and the initial radius of the solid target is 200 μm, which corresponds qualitatively to the degree of laser beam defocusing. The waveform of the laser pulse was similar to the actual one. Let us point out certain characteristic features of the curves shown in Fig. 4. First, the intensities of both the resonant and intercombination lines are maximum when the electron density substantially exceeds the critical density. This explains the high intensity of soft X radiation observed in the experiments. Second, the radiation in the resonant lines and satellites is emitted from different regions of the plasma. Thus, the maximum of emission intensity in the resonant lines is observed for an electron temperature of 200 eV, whereas the maximum population of a Li-like ion corresponds to a temperature of nearly 50 eV. The region in which the Li-like ions can exist is very narrow (about 20 μm), which agrees well with the fact that, in the experiment, the satellites of the resonance lines of He-like Mg ions are seen only on the target surface (Fig. 2). We should mention that the intensity of the satellites is affected not only by strong inhomogeneity of the plasma, but also by suprathermal electrons that are present in the plasma [8, 9]. In both the experiment and the calculations, the intensity of the resonant line of hydrogen-like ions was at a level of 10^{-2} of the intensity of the resonant lines of He-like ions. This allows us to conclude that, near the target, the ion are mainly in the He-like state.

Figure 1 demonstrates the experimental and calculated ion distributions over the degree of ionization; the experimental distributions are reconstructed from the energy spectrum measured at a distance of 3 m from the target with the help of an electrostatic analyzer. Both in the experiment and the calculations, the most abundant ions are He-like magnesium ions. The difference in the distributions for low degrees of ionization may be attributed to the nonisotropic angular distribution of the ion density, the influence of a "wing" in the laser intensity distribution, and the recombination of the plasma in the drift space.

In summary, the combination of space-resolved X-ray spectral measurements and the time-of-flight technique has allowed us to simultaneously determine

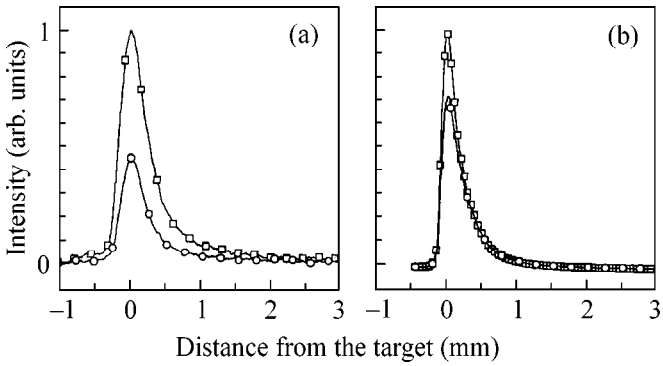

Fig. 3. (a) Experimental and (b) calculated intensities of the resonant and intercombination lines as functions of the distance from the target.

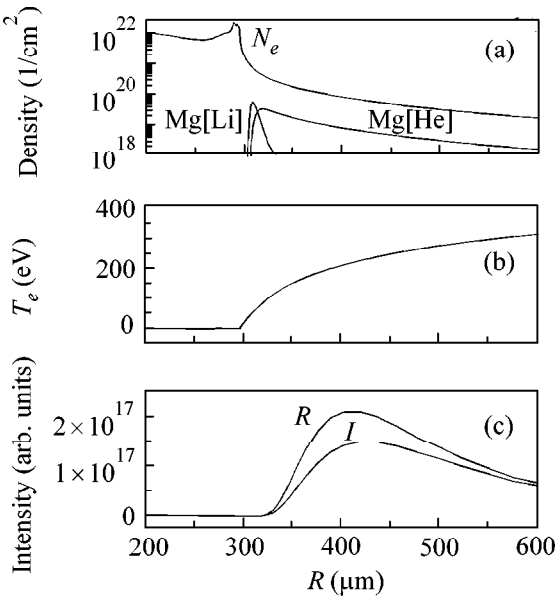

Fig. 4. Spatial distribution of the plasma parameters at the instant of the maximum laser power for R = 200 μm and $P_0 = 6.25 \times 10^{12}$ W/cm^2: (a) the electron density N_e and the densities of Li- and He-like magnesium ions; (b) the electron temperature T_e; and (c) volume emission intensity in the resonant line of He-like Mg ions (R[He]) and intercombination line of He-like Mg ions (I[He]).

the ion composition of a laser plasma both near the target and at a large distance from it.

This work was supported in part by the INTAS, project no. 2090-97.

REFERENCES

1. S. V. Khomenko, R. N. Makarov, V. C. Roerich, *et al.*, Preprint No. 0045-A, TRINITI (Troitsk Institute of Innovation and Fusion Research, Troitsk, 1998).
2. I. Yu. Skobelev, A. Ya. Faenov, B. A. Bryunetkin, *et al.*, Zh. Éksp. Teor. Fiz. **108**, 1263 (1995) [JETP **81**, 692 (1995)]; D. A. Pikuz, A. Ya. Faenov, S. A. Pikuz, *et al.*, J. X-Ray Sci. Technol. **5**, 323 (1995); A. Ya. Faenov, S. A. Pikuz, A. I. Erko, *et al.*, Phys. Scr. **50**, 333 (1994).
3. A. E. Stepanov, A. N. Starostin, V. C. Roerich, *et al.*, J. Quant. Spectrosc. Radiat. Transfer **58**, 937 (1997).
4. A. L. Godunov, V. A. Makhrov, A. Yu. Sechin, *et al.*, Zh. Éksp. Teor. Fiz. **109**, 2064 (1996) [JETP **82**, 1112 (1996)].
5. G. B. Rybicki and D. G. Hummer, Astrophys. J. **274**, 380 (1983).
6. J. Nilsen, P. Beiersdorfer, S. R. Elliot, *et al.*, Phys. Rev. A **50**, 2143 (1994).
7. S. Bollanti, P. Di Lazzaro, F. Flora, *et al.*, Phys. Scr. **51**, 326 (1995).
8. J. Abdallah, Jr., A. Ya. Faenov, D. Hammer, *et al.*, Phys. Scr. **53**, 705 (1996); J. Abdallah, Jr., A. Ya. Faenov, T. A. Pikuz, *et al.*, J. Quant. Spectrosc. Radiat. Transfer **62**, 1 (1999); J. Abdallah, Jr., R. E. H. Clark, A. Ya. Faenov, *et al.*, J. Quant. Spectrosc. Radiat. Transfer **62**, 85 (1999).
9. F. B. Rosmej, J. Quant. Spectrosc. Radiat. Transfer **51**, 319 (1994); F. B. Rosmej and O. N. Rosmej, AIP Conf. Ser. **299**, 560 (1994); F. B. Rosmej, A. Ya. Faenov, T. A. Pikuz, *et al.*, JETP Lett. **65**, 708 (1997).

Translated by N. Larionova